Supplementary Materials

Enhancing the activity of oxygen-evolution and chlorine-evolution electrocatalysts by atomic layer deposition of TiO_2

Authors: Cody E. Finke[1,2,3]*, Stefan T. Omelchenko[3], Justin T. Jasper[1,2], Michael F. Lichterman[4], Carlos G. Read[2,4], Nathan S. Lewis[4], Michael R. Hoffmann[1,2,3,*]

Affiliations:

[1]The Linde Center for Global Environmental Science, Caltech, Pasadena, CA 91125, USA.

[2]The Resnick Sustainability Institute, Caltech, Pasadena, CA 91125, USA.

[3]Division of Engineering and Applied Science, Caltech, Pasadena, CA 91125, USA.

[4]Division of Chemistry and Chemical Engineering, Caltech, Pasadena, CA 91125, USA.

*Corresponding Authors: finkec@caltech.edu, mrh@caltech.edu

Table of Contents

Surface Topography Determinatiion and Surface Homogeneity, and Acitve Site Discussion

Transmission Electron miscroscopy

To better understand the surface morphology, TEM images were aquired of 10 and 40 ALD cycles of TiO_2 on IrO_2. Transmission-electron microscopy (TEM) samples of films were prepared using a focused Ga-ion beam (FIB) on a FEI Nova-600 Nanolab FIB/FESEM, with Pt and C protection layers being applied before being exposed to the FIB. High-resolution TEM (HRTEM) images and high-angle annular dark-field scanning transmission electron microscopy (HAADF-STEM) images were collected on an FEI Titan G2 S/TEM equipped with spherical aberration correctors on the image and probe-forming lenses at an accelerating voltage of 200 kV. STEM-EDS maps were acquired in the FEI Titan using the Super-X EDX quad detector system at a current of 0.1 nA. Standard-less Cliff-Lorimer quantification was performed on the deconvoluted EDS line intensity data using the Bruker Esprit software. Fig. S1 below shows HAADF-STEM images of 10 cycles of TiO_2 exhibited a semicontinuous film where the majority of imaged areas were covered withTiO_2 with relatively small gaps of what appeared to be uncoated area. 40 ALD cycle exhibited a fully continuous film for at all areas imaged.

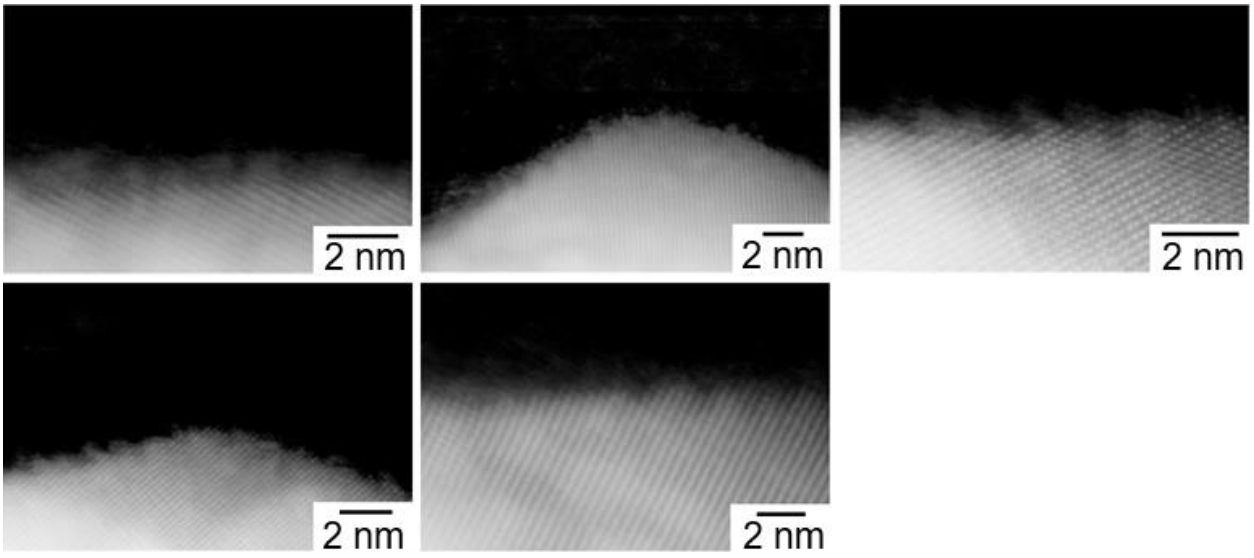

Fig. S1. High-Angle Annular Dark-Field Scanning Transmission Electron Microscopy (HAADF-STEM) images of different IrO_2 + 10 ALD cycles of TiO_2 samples. The crystalline sublayer is IrO_2 and the hairy top layer is amorphous TiO_2.

Atomic Force Microscopy

Atomic Force Microscopy (AFM) was used to investigate the surface morphology. A Bruker Dimension Icon was used in Peak Force Tunneling AFM Mode (PF-TUNA) for all topography and conductive AFM measurements. Representative surface topology (Fig. S2) and conductive AFM (TUNA current) (Fig. S3) for 0, 3, 10, and 1000 ALD TiO_2 cycles are shown for IrO_2, RuO_2, and FTO substrates. AFM images of RuO_2, IrO_2, FTO, and substrates coated with 1000 cycles of TiO_2 were consistent with previously reported images of materials grown under similar conditions [1-4].

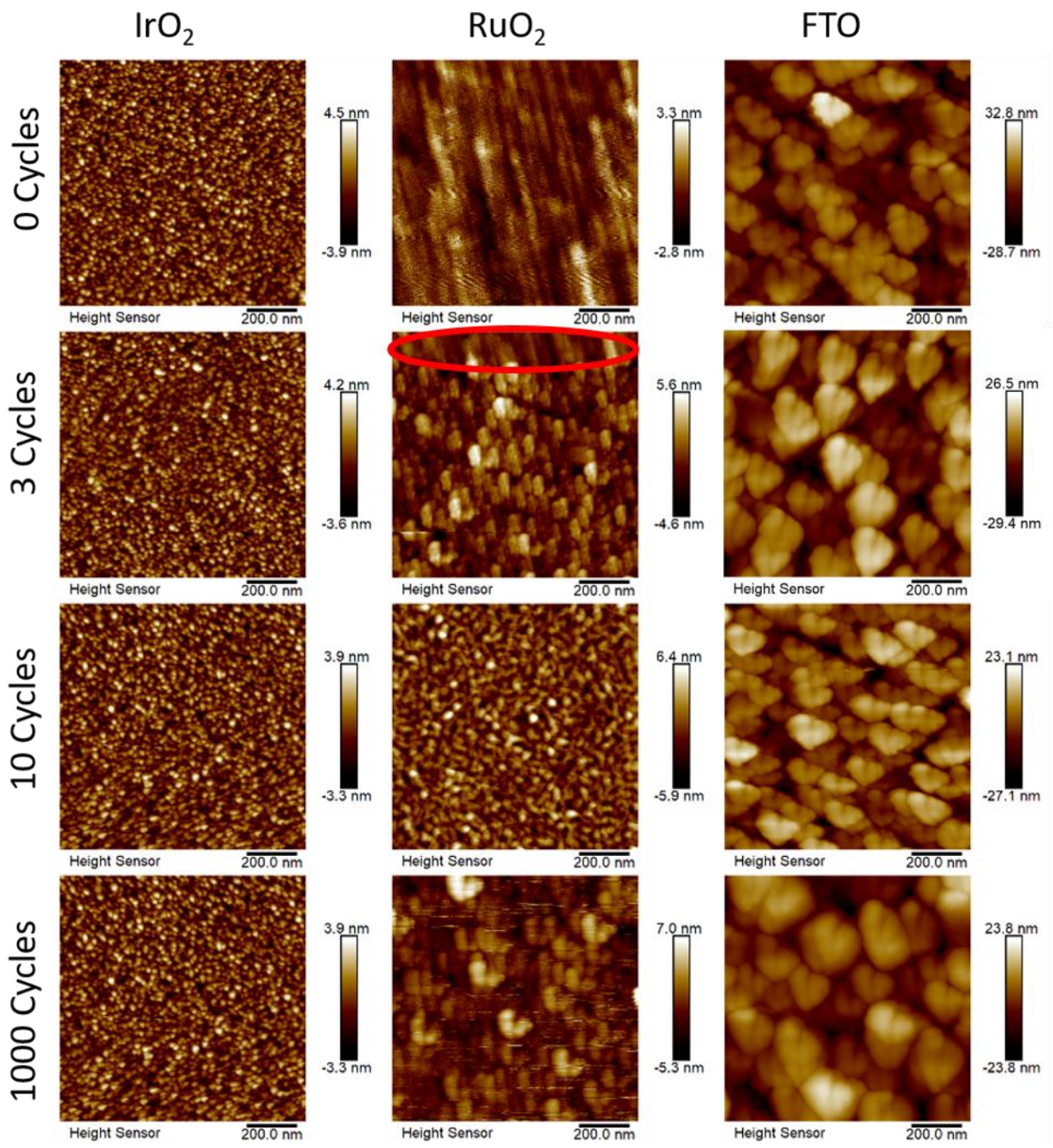

Fig. S2. Representative topographic atomic force microscopy images of IrO_2, RuO_2, and FTO each with 0, 3, 10, and 1000 ALD cycles of TiO_2. The red cirle indicates exposed RuO_2 under TiO_2.

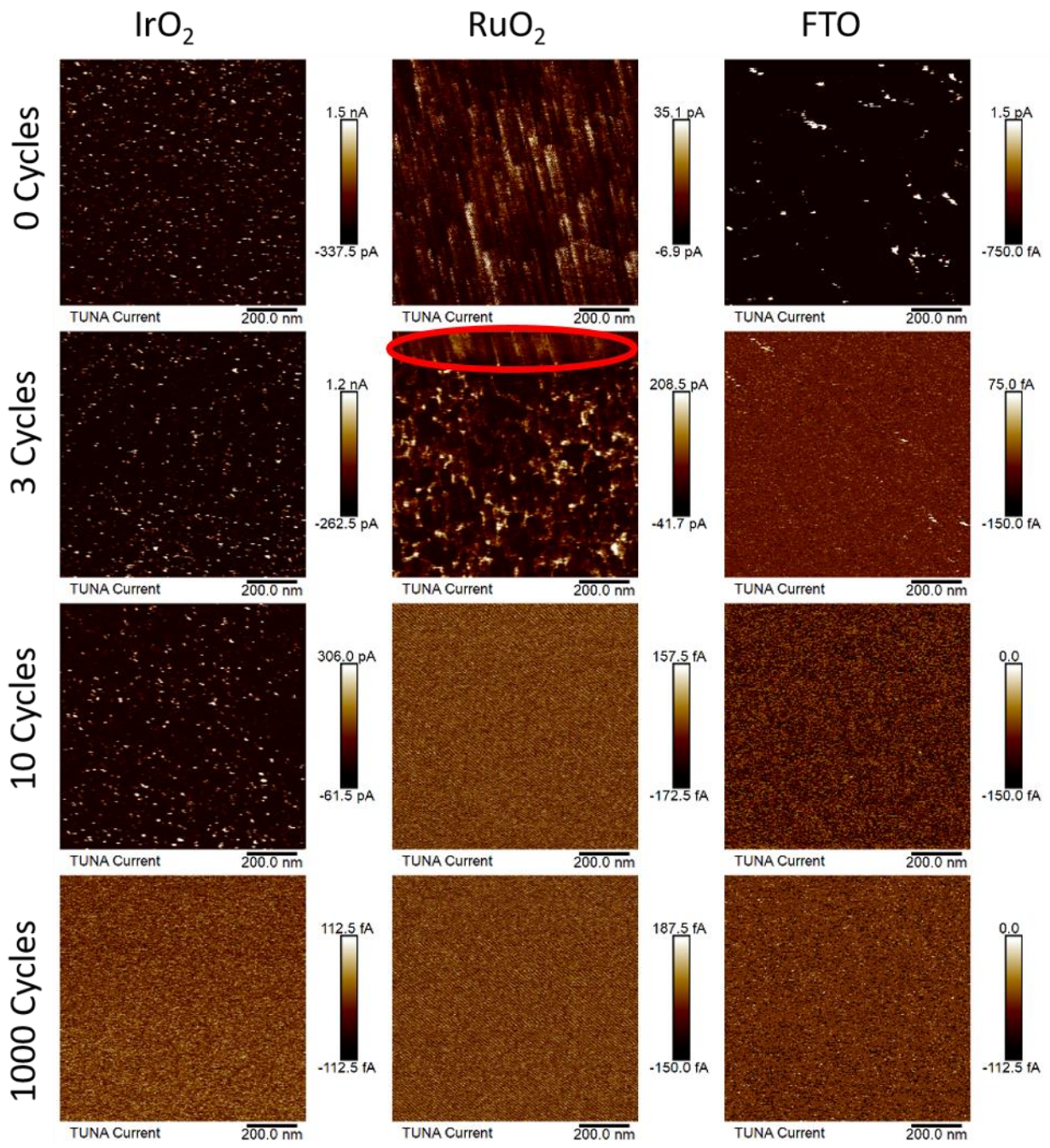

Fig. S3. Representative conductive atomic force microscopy tunneling current images of IrO_2, RuO_2, and FTO each with 0, 3, 10, and 1000 ALD cycles of TiO_2. The red cirle indicates exposed RuO_2 under TiO_2.

Table S1. Surface area (measured by AFM) as a percent of geometric surface area. Dividing these values by 100 yields topographic roughness factors.

	AFM Measured Surface Area as a Percentage of Geometric Surface Area		
TiO_2 Cycle Number	**IrO_2**	**RuO_2**	**FTO**
0	104.52%	107.75%	108.35%
3	103.87%	102.45%	107.98%
6	103.12%	103.93%	110.24%
10	102.94%	104.08%	108.05%
20	103.32%	104.61%	110.60%
30			108.92%
40	102.70%	102.61%	108.27%
50			108.18%
60	103.60%	101.65%	108.10%
500	102.00%		
1000	102.01%	111.02%	104.15%

The surface area as measured by AFM was at most 112% of the geometric surface area (Table S1). It was very difficult to find places in AFM images where the underlying material was exposed even at only 3 ALD cycles of TiO_2. On FTO and IrO_2, the base electrocatalyst materials did not appear to be exposed even at 3 ALD cycles. However, for RuO_2, while mostly the sample appeared to be covered by TiO_2, there was some evidence of holes in the TIO_2 coverage, and we chose to display that image. For IrO_2 and FTO, the surface topography was similar for all cycle numbers of TiO_2. The only observable change as the number of ALD cycles increased was that the conductivtiy and surface area decreased uniformly as TiO_2 was deposited, suggesting that TiO_2 coated the catalysts' surface reasonably evenly, see Fig. S1 for TEM images for higher resolution coverage analysis. Based on AFM data, No holes were visible in the TiO_2 coating at any cycle number for FTO and IrO_2. The surface topography of bare RuO_2 was rippled (0 cycles), and gradually morphed into a flake-like structure (3-6 cycles), a columnar structure similar to IrO_2 (10-30 cycles), and then back into flakes similar to FTO (>30 cycles). Furthermore, for RuO_2 at 3 ALD cycles some holes in the TiO_2 were clearly visible in both the topological and the conductive

AFM images. No such holes were visible at > 3 cycles TiO_2. Conductive AFM showed uniformly drecreasing conductivity with cycle number once no holes were visible (>3 cycles TiO_2).

Profilometry

Profilometry was performed on a Bruker DektakXT Stylus profilometer. TiO_2 ALD growth rates on FTO were determined by masking a portion of the FTO sample with Dupont Kapton Tape (Dupont, WA) and then using the profilometer to scan across the TiO_2 boundary after deposition. A 1000 cycle sample was scanned 3 times and the TiO_2 thickness was determined to be 50.8 ± 2.1 nm. The growth rate was therefore ~0.5 Å/ALD cycle, assuming that growth was linear, which corroborates previously reported gowth rates measured using the same ALD recipe on the same instrument [5].

Scanning Electron Miscroscopy

Scanning electron micrographs (SEMs) were obtained with a FEI Nova NanoSEM 450 at an accelerating voltage of 5.00 kV with a working distance of 5 mm and an in-lens secondary electron detector**.** Based on cross-sectional SEM images of films subjected to 1000 cycles of ALD, linear growth rates were estimated to be ~0.65 Å/ALD cycle (Fig. S4), in reasonable agreement with profilometry results as well as with previously measured growth rates [5].

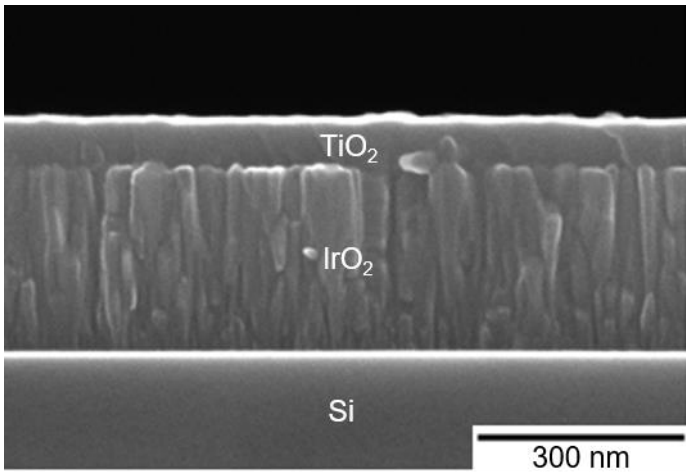

Fig. S4. A cross-sectional SEM image of a sample consisting of a silicon wafer substrate sputter coated with IrO_2 and then overcoated with 1000 cycles of ALD TiO_2.

Active Site:

The data presented in this paper do not conclusively determine an active site. The active sites on each catalyst may be different for the CER and OER. Previous studies have shown that both OER and CER can occur on SnO_2, TiO_2, RuO_2, and IrO_2 which indicates that all materials may adsorb water and function as an active site[6-9]. In general, it is believed that OER active sites on active metal oxides involve either a protonated oxygen ligand or a coordinatively unsaturated metal. The CER is believed to occur either at the same active site as the OER or via a displacement reaction with a surface bound hydroxide. There is substantial spectroscopic and chemical evidence for oxygen protonation on TiO_2 indicating that, like SnO_2, IrO_2 and RuO_2, TiO_2 may adsorb water[10-13] indicating that if the electron density of the TiO_2 were to be tuned just right, then it could act as an active site.

In this work, we see enhanced activity and corresponding changes in surface electron density when TiO_2 is added and then that enhanced activity goes away when the TiO_2 is removed (Fig. S7). TEM images of samples with 10 or more cycles of TiO_2 (Figs 1 and S1) show near complete coverage of the surface and AFM of samples with more than 3 cycles of TiO_2 corroborate this evidence. If TiO_2 were not part of the active site, we might expect that the electrochemically active surface area would decrease substantially when the underlying material is covered, however we do not see a substantial decrease in ECSA for any of the materials with fewer than 40 cycles of TiO_2. In summary, AFM and TEM images indicate that TiO_2 is covering the vast majority of the surface for all reasonably active catalysts, there is evidence that TiO_2 can adsorb water and evolve O_2 and Cl_2, and the ECSA does not meaningfully decrease when the surface is coated with TiO_2. These pieces of evidence are most consistent with TiO_2 being involved in the active site.

Estimation of Electronegativity:

Electronegativities were estimated for heterogeneous electrocatalysts by taking the geometric mean of the electronegativities of the constituent atoms [14, 15]. Allen scale electronegativities were used because this scale is better than other electronegativity scales (e.g. Pauling, Mulliken, Allred-Rochow) at differentiating between the electronegativities of the transition metals [16-18]. As an example, for TiO_2: Ti ($\chi = 1.38$) and O ($\chi = 3.61$), therefore TiO_2 ($\chi \approx (1.38 \times 3.61^2)^{1/3} = 2.62$). In the case of FTO, the electronegativity of SnO_2 was estimated because it is not known how small quantities of F would change the electronegativity of SnO_2. Electronegativity is a useful theoretical concept for estimating the directions in which surface charge availability and the corresponding catalyst-reacting-species bond strength may move, but not to estimate the magnitude of change or any complex details of any physical parameter.

To better understand how group electronegativities may be correlated with catalytic activity for heterogeneous electrocatalysts, group electronegativities were calculated for oxygen evolution catalysts from this work and for the catalysts compared in Seh *et al.* and plotted against overpotentials at 1 mA/cm^2_{AFMSA} for each catalyst. Like in Seh *et al*., for catalysts with no AFM data, if they were prepared on flat substrates (e.g. (100) silicon), a roughness factor of 1 was assumed. (Fig. S5)[19]. In the case of catalysts with undefined elemental ratios, XPS data on the oxidation state was used to estimate elemental composition, and then fractional compositions were rounded to the nearest half. If there was no XPS data, Pourbaix diagrams were consulted and the predominant species at the relevant potentials were used for group electronegativity calculations. In most cases, assumptions were the same as the assumptions made for active site composition in Seh *et al*[19]. For layered catalysts (e.g. $IrO_x/SrIrO_3$) the geometric mean of all the atoms in the overlayer and underlayer was used as the group electronegativity of the material. Overpotentials at 1 mA/cm^2_{AFMSA} was either taken from Seh *et al*[19]*.* or from this work. Most overpotential data presented in Fig. S5 was collected in a basic electrolyte (blue circles), for catalysts tested in acidic electrolytes, red circles indicate values from this work measured in 1 M H_2SO_4 and the orange circle indicates the catalyst tested in 0.5 M H_2SO_4 from Seitz *et al.* [20]. Electronegativity, like other theoretical constructs that are related to bond strength, demonstrates a nice volcano type correlation with activity for the oxygen evolution reaction [20]. These data presented in Fig. S5 below and the data presented in Fig. 2 of the main text, indicate that group electronegativity may be a simple and useful tool to choose candidates for heterogeneous electrocatalysts. No Allen Scale electronegativity exists for Lanthanum so the geometric mean of

Barium and Lutetium (the most adjacent atoms to Lanthanum with known Allen Scale electronegativities) was used instead resulting in an $\chi_{La} = 0.98$.

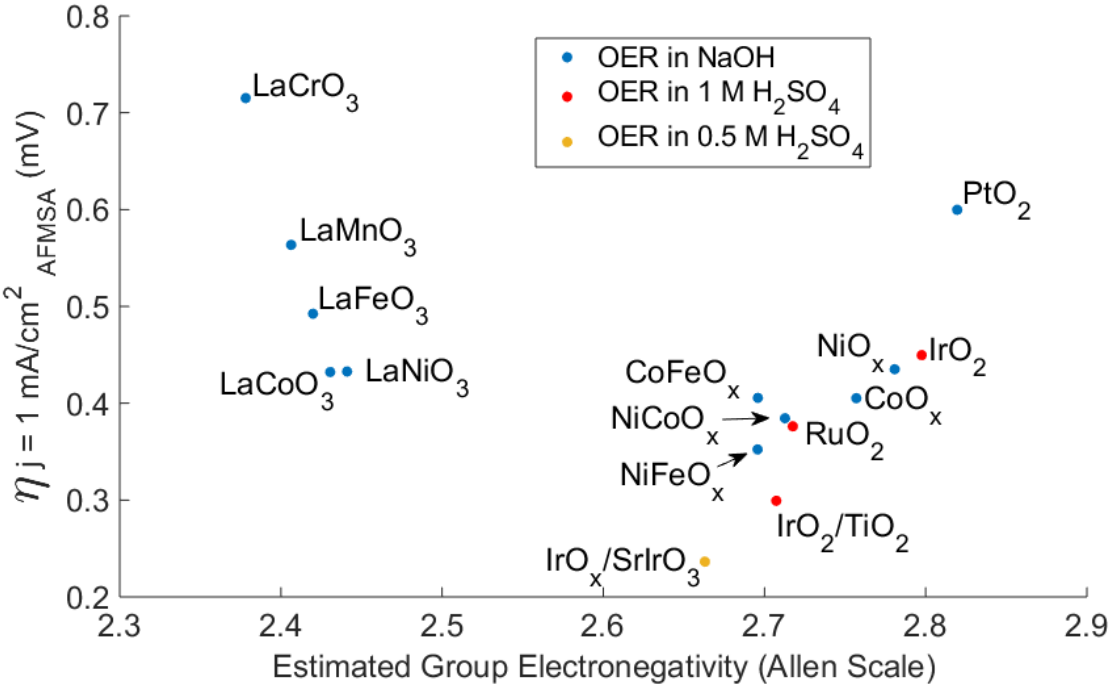

Fig. S5. Group electronegativity vs overpotential at 1 mA/cm^2_{AFMSA}. Overpotential data was taken from Seh *et al.* (blue and orange circles) and from this work (red circles). For $LaCrO_3$, $LaMnO_3$, $LaFeO_3$, $LaCoO_3$, $LaNiO_3$, RuO_2, IrO_2, and PtO_2 group electronegativites were estimated by taking the geometric mean of the Allen Scale electronegativities of the constituent atoms. For $IrO_x/SrIrO_3$, Ir_2SrO_7 was assumed for group electronegativity calculations [20]. For IrO_2/TiO_2, $IrTiO_4$ was assumed for group electronegativity calculations For $NiFeO_x$, $NiFe_2O_4$ was was assumed for group electronegativity calculations [21]. For $NiCoO_x$ $NiCo_2O_4$ was assumed for group electronegativity calculations [21]. For $NiCoO_x$, $NiCo_2O_4$ was assumed for group electronegativity calculations [21]. For $CoFeO_x$, $FeCo_2O_4$ was assumed for group electronegativity calculations [21]. For CoO_x, $CoO_{1.5}$ was assumed for group electronegativity calculations [21]. For NiO_x, Ni_2O_3 was assumed for group electronegativity calculations [21].

Electrode Preparation:

RuO_2 and IrO_2 Sample Preparation

(100) oriented, boron doped, < 0.01 Ω-cm, 525 ± 25 μm thick p^+-Si wafers were obtained from Addison Engineering (San Jose, CA). Wafers were cleaned for 1 min in buffered HF (Transene, Danvers, MA, used as received) and then immediately put under a vacuum of < 7 x 10^{-6} Torr. ~300 nm of RuO_2 or IrO_2 were deposited on the wafer using an AJA International Inc. (Scituate, MA) Orion sputter-deposition system equipped with Phase II-J software. Samples were heated to 300 ^oC and Ir or Ru were sputtered using an RF source under an Ar/O_2 plasma with a constant flow of 20 sccm Ar and 3 sccm O_2 for 22.42 min for Ir, and 13.5 sccm Ar and 1.5 sccm O_2 for 22 min for Ru. The chamber pressure was maintained at 5 mTorr during deposition, and the base pressure of the chamber was held at < 10^{-7} Torr between depositions. The phase purity of the samples was confirmed by X-ray diffraction measurements, as detailed below (Fig. S6).

Following ALD of TiO_2 (see below), a tungsten-carbide-tipped scribe was used to contact a gallium-indium eutectic (Alfa Aesar, Ward Hill, MA, 99.99%, used as received) onto the back side of the IrO_2 and RuO_2 samples. A coiled zinc-plated copper wire (Consolidated Electrical Wire and Cable, Franklin Park, IL) was placed onto the gallium-indium and the wire was covered with one-sided copper foil tape (3M, Maplewood, MN, used as received).

XRD crystal structures of the IrO_2 and RuO_2 substrate are shown in Fig. S6 below.

FTO Sample Preparation

Tec 15 FTO glass slides (Hartford Glass Co., Hartford City, IN) were broken into ~1 cm^2 pieces. The FTO pieces were then washed in a sonication bath in acetone, isopropyl alcohol, and deionized water, sequentially, for 15 min at each step. ALD of TiO_2 was performed as described below. A coiled zinc-plated copper wire (Consolidated Electrical Wire and Cable) was placed onto the conductive side of the FTO electrode and secured with one-sided copper foil tape.

To protect the contact and define the geometric surface area, circular holes were punched in a strip of 1-inch width 3M vinyl electroplating tape using a 2 or 3 mm diameter circular punch. The entire electrode was then covered with this tape, only exposing the 3 mm diameter circle of the electrode. The wire covered the tape for at least 4 cm, such that neither the wire housing nor the

metallic wire was exposed to the electrolyte. After testing, electrodes were inspected for leaks and then disassembled and the copper contacts were checked for corrosion to ensure no leaking. Baseline and peak overpotentials were confirmed during stability testing using epoxy sealed electrodes (Table S3).

Atomic Layer Deposition

TiO_2 films were deposited on IrO_2, RuO_2 and FTO at 150 °C using an Ultratech Fiji 200 Plasma ALD System (Veeco, Waltham, MA). The IrO_2, RuO_2, and FTO were prepared as described above. Prior to ALD, one 0.060 sec pulse of H_2O was applied to the sample. Each ALD cycle consisted of a 0.250 sec pulse of tetrakis(dimethylamido)titanium (TDMAT, Sigma-Aldrich, St. Louis, MO, 99.999%, used as received), followed by a 0.060 sec pulse of H_2O (18 MΩ cm, Millipore). A 15 sec purge under a constant 0.13 L/min flow of research-grade N_2 was performed between each precursor pulse. While idle, the ALD system was maintained under a continuous N_2 purge with a background pressure of 0.50 Torr.

X-Ray Diffraction

X-ray diffraction (XRD) measurements were performed with a Bruker D8 Discover equipped with a 2-dimensional Vantec-500 detector. Copper K_α radiation (1.54 Å) was generated with a tube voltage of 50 kV and a tube current of 1000 μA. The incident beam was focused with a 0.5 mm diameter mono-capillary collimator. An aligned laser beam was used to ensure that the sample was placed at the correct depth for diffraction measurements. Coupled theta/two-theta mode was used. The scattered X-ray radiation was collected by the Vantec-500 detector with an angular resolution < 0.04°, which enabled the collection of diffraction from a 2θ range of 20°. To obtain the XRD profile, four scans were performed in the range of 10° to 90° 2θ, and radiation was counted for a total duration of 1 h. The collected data were analyzed using Bruker EVA software. All observed peaks were indexed to standard diffraction patterns for IrO_2 and RuO_2, respectively, from the Inorganic Crystal Structure Database [22, 23].

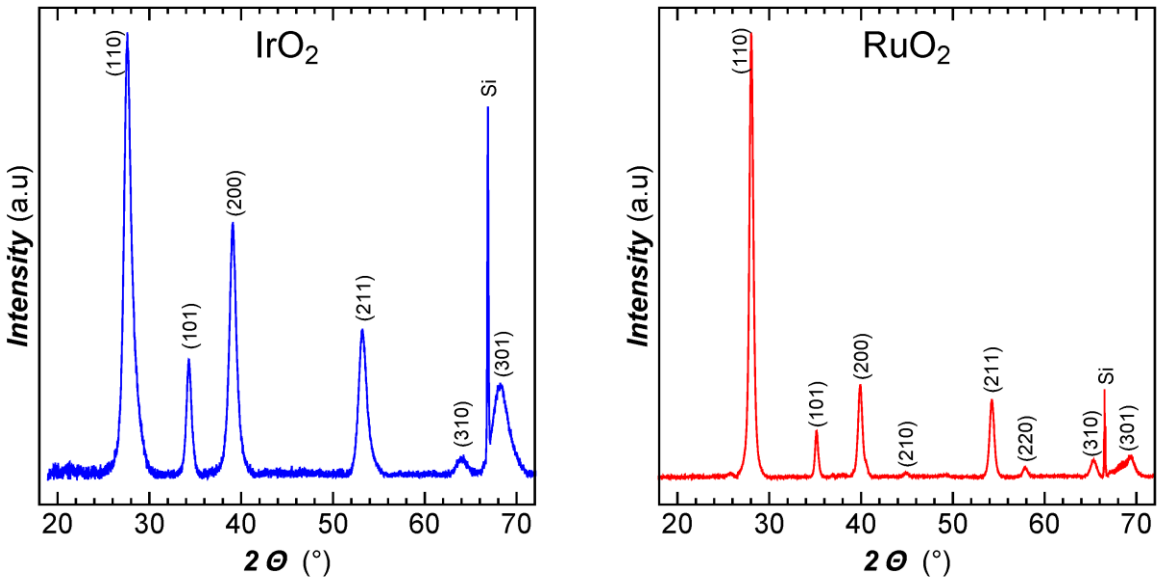

Fig. S6. X-ray diffraction patterns for typical IrO_2 and RuO_2. All observed peaks were indexed to standard diffraction patterns for IrO_2 and RuO_2, respectively.

Electrochemical measurements

With assistance from a large-gauge needle guide, the lead of each electrode was inserted through a rubber septum, and the electrode was placed in a 25 mL, 14/20, 4-necked, round bottom flask (Chemglass, Vineland, NJ). The flask was filled with 15 mL of 1.0 M H_2SO_4 or 5.0 M NaCl at pH 2.0 (adjusted using HCl and measured using a calibrated Thermo Scientific Orion 3 Star pH probe). A saturated calomel electrode (SCE; CH Instruments, Austin, TX) reference electrode was washed and placed in the solution.

For OER and CER experiments, O_2(g) or Cl_2(g) was flowed through a bubbler that contained either 1.0 M H_2SO_4 or 5.0 M NaCl at pH 2.0, respectively, and then into the reactor using a Teflon tube that extended ~1 cm below the surface of the electrolyte. To ensure that the reactor was pressurized to 1 atm, gas could freely escape through an identical Teflon tube that went from the reactor flask to the back of the fume hood. Prior to data collection, the gas was bubbled through the solution for > 1 min. The counter electrode was a 0.5 mm diameter coiled platinum wire (Sigma Aldrich, 99.9%). All purging and experiments were performed under continuous stirring. The distance between the working electrode and reference electrode was 1.0 cm.

To measure overpotential, the following experiments were run on a Bio-Logic (Seyssinet-Pariset, France) potentiostat/galvanostat model VSP-300 with EIS capability:

1) Open circuit voltage for 30 sec.

2) Two cyclic voltammograms (CVs) to clean the electrode, scanning from 1.0 to 1.45 vs SCE for RuO_2 and IrO_2 in 1.0 M H_2SO_4 (prior to OER); from 1.2 to 1.8 vs SCE for FTO in 1.0 M H_2SO_4 (prior to OER); from 1.1 to 1.2 V vs SCE for RuO_2 and IrO_2 in 5.0 M NaCl at pH 2.0 (prior to CER); and from 1.1 to 2.0 V for FTO in 5.0 M NaCl at pH 2.0 (prior to CER).

3) Hold the potential at open circuit for 30 sec.

4) Two CVs to measure the overpotential, scanning from 1.0 to 2.5 vs SCE for RuO_2 and IrO_2 in 1.0 M H_2SO_4 (OER), 1.5 to 3.5 for FTO in 1.0 M H_2SO_4 (OER), 1.1 to 1.35 V vs SCE for RuO_2 and IrO_2 in 5.0M NaCl at pH 2.0 (CER), and for 1.1 to 3.0 V FTO in 5.0 M NaCl at pH 2.0 (CER).

All CVs were conducted at a 5 mV/sec scan rate and were corrected for solution resistance as described below, unless otherwise stated. The system resistance was also measured for each sample prior to each experiment. For each electrode, at least 4 replicates were tested.

Overpotential Calculations

For the OER, standard conditions were assumed, and the thermodynamic potential of 1230 mV vs RHE was used to determine the OER overpotential at 10 mA/cm^2.

For the CER, the activity for Cl^- was estimated to be 4.36 using the Pitzer model [24] and the fugacity of 1 atm Cl_2 was taken to be 0.07267 [25]. Using these values, a thermodynamic potential of 1288 mV vs NHE was calculated from the Nernst equation.

Faradaic Efficiency Determination

For the OER, the faradaic efficiency of the electrodes was measured as previously described using a pneumatic trough [26]. A graduated cylinder was filled with electrolyte and placed upside down in a bath of electrolyte. The working electrode was inserted to a height > 1 cm into the cylinder. The reference electrode was placed near the cylinder and the counter electrode was placed > 5 cm away from the cylinder. The cylinder was closed to the bulk solution except for the pour spout of the cylinder, hence ions were allowed to pass freely. The electrode was biased to pass 10 mA of current at 10 mA/cm$^2_{geo}$, and the resulting oxygen bubbles were collected in the

cylinder for 1 h. The resulting head-space volume was measured and compared using the ideal gas law to the expected total charge passed. Similar to other studies, 105-115% faradaic efficiencies were measured (Table S2). The excess is attributed to electrolyte sticking to the cylinder walls, narrowing the diameter of the cylinder.

For the CER, electrodes were operated at a constant current of 1mA/cm^2_{geo} for 10 min in 15 mL of 5.0 M NaCl at pH 2.0, which, given 100% faradaic efficiency, should yield 22.08 ppm Cl_2(g) in our experimental configuration. Immediately after the reaction, one milliliter of electrolyte was transferred to a 25 mL beaker and chlorine was measured by titrating excess potassium iodide with a starch indicator using 0.50 mN $Na_2S_2O_3$ [27]. Greater than 90% faradaic efficiency was measured for samples with 40-60 ALD cycles of TiO_2 and greater than 95% faradaic efficiency was measured for samples with fewer than 40 ALD cycles of TiO_2 (Table S2).

Table S2. Faradaic efficiencies for the OER and CER.

	OER			**CER**		
TiO_2 Cycle Number	**IrO_2**	**RuO_2**	**FTO**	**IrO_2**	**RuO_2**	**FTO**
0	108%	122%	114%	101%	95%	97%
1			86%	96%	99%	102%
3	120%	122%	97%	99%	96%	96%
6	120%	107%	103%	101%	96%	98%
10	114%	122%	114%	96%	99%	96%
15		114%				
20	117%	122%	114%	104%	95%	98%
25			114%			
30	120%	114%	114%			
40	108%	114%	114%	95%	91%	91%
50	103%	114%				
60	120%	114%	103%	91%	95%	113%
100	114%	107%	114%	92%	91%	15%

24-h Stability Testing

For this study, the catalysts were optimized to remove effects of surface roughness that could lead to artificially high activity. Thin films of IrO_2 and RuO_2 prepared using nominally identical procedures to the one used herein exhibit degradation in less than 1 h[21, 28]. The rapid degradation of these catalysts allowed us to quickly determine whether the addition of TiO_2 affected the stability of the catalyst. In the benchmarking study, when thicker catalyst coatings of identically prepared IrO_2 and RuO_2 were used, the catalyst stability improved[21, 28].

For each catalyst, the uncoated and the most active, coated catalysts were tested for 24 h stability. For the OER, IrO_2 with 40 ALD cycles of TiO_2 was also tested. 10 mA/cm^2 in 1 M H_2SO_4 Electrodes were as prepared as described above except, instead of vinyl tape, electrode surface area was defined by Hysol 9460 epoxy (Henkel, Dusseldorf, Germany) [20]. Geometric surface areas were measured as previously described by scanning the electrode surface using a Ricoh MP 301 scanner (Tokyo, Japan) and estimating the surface area using ImageJ software [20]. The catalyst stability was assessed by maintaining the electrodes galvanostatically at either 10 mA/cm^2 or 1 mA/cm^2 for the OER and CER, respectively, for 24 hrs. At 0 min, 10 min, 2 h, and 24 h, the electrolyte was replaced with fresh electrolyte, and either O_2(g) or Cl_2(g) was bubbled through the solution as described above. After > 1 min of gas bubbling, electrochemical impedance spectroscopy was preformed to determine the system resistance followed by 5 CVs which were run from the OCV to a potential that yielded 10 mA/cm^2 or 1 mA/cm^2 for the OER and CER, respectively. The voltage required to reach 10 mA/cm^2 for the OER and 1 mA/cm^2 for the CER, respectively, is tabulated in Table S3 below. Initial overpotential measurements agree well with overpotential measurements using vinyl tape on electrodes reported in Fig. 1 (Table S3). In general, for the OER small cycle numbers of TiO_2 (≤ 10) extended the lifetime of the catalysts from <1 h to <4 h and thicker coatings (≥ 30) extended the catalyst lifetime to > 7 h. As previously reported for thin IrO_x catalysts for the OER, the overpotential to reach 10 mA/cm^2 rapidly increased after < 1 h of testing. For the CER, all catalysts were reasonably stable over the 24 h testing period except for the less stable FTO catalysts which followed a similar pattern as OER catalysts. A sample 24 h stability test of 0, 10, and 40 ALD cycles of TiO_2 on IrO_2 under OER conditions is presented in Fig. S7 below.

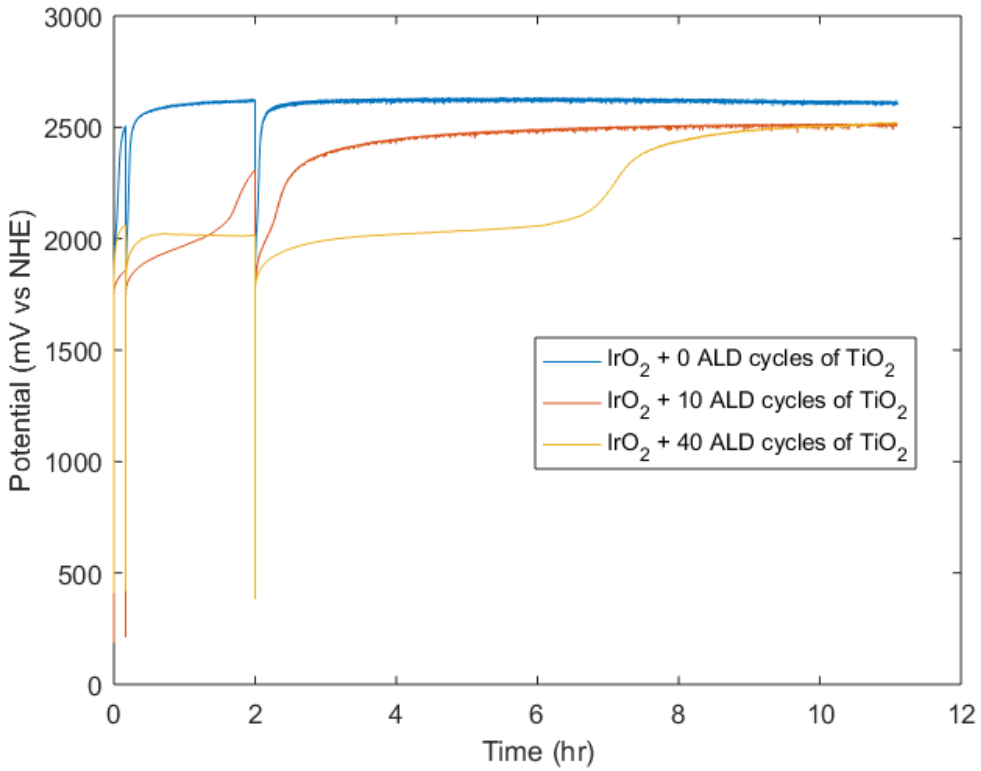

Fig. S7. Example stability testing data of IrO_2 + 0 (blue), 10 (orange), and 40 (yellow) ALD cycles in 1 M H_2SO_4 at 10 mA/cm^2_{geo}.

Table S3. Summary of overpotential data as measured from CVs to reach 10 mA/cm$^2_{geo}$ in 1 M H_2SO_4 for the OER and 1 mA/cm$^2_{geo}$ in 5 M NaCl pH 2.0 for CER at 0 min, 10 min, 2 h, and 24 h of testing in constant current mode. The right-most column displays the overpotential that was reported in the main text. N/A indicates that a rapid loss in activity was noticed before the time of measurement.

OER overpotential to reach 10 mA/cm$^2_{geo}$					
MO_x + X ALD Cycles of TiO_2	initial	10 min	2 h	24 h	Reported initial value (Fig. 1.)
IrO_2 + 0 cyc	720	670	N/A	N/A	710 ± 30
IrO_2 + 10 cyc	540	510	N/A	N/A	520 ± 20
IrO_2 + 40 cyc	800	610	560	N/A	810 ± 50
RuO_2 + 0 cyc	770	880	N/A	N/A	740 ± 70
RuO2 + 10 cyc	430	470	440	N/A	430 ± 10
FTO + 0 cyc	1870	1820	N/A	N/A	1870 ± 50
FTO + 30 cyc	1740	1620	N/A	N/A	1720 ± 70
CER overpotential to reach 1 mA/cm$^2_{geo}$					
IrO2 + 0 cyc	160	220	230	N/A	148 ± 6
IrO2 + 3 cyc	120	200	200	190	122 ± 5
RuO2 + 0 cyc	140	220	140	210	116 ± 6
RuO2 + 60 cyc	160	160	100	100	160 ± 10
FTO + 0 cyc	870	980	990	970	890 ± 30
FTO + 10 cyc	760	1150	1000	740	760 ± 40

Determination of Solution and System Resistance

The solution resistance was estimated using electrochemical impedance spectroscopy on a coiled Pt wire working electrode and Pt wire counter electrode system. The wire coil was 3 mm in diameter to simulate the working electrode and was placed 1 cm from the SCE reference electrode to simulate the distance between working and reference electrode. Measurements were taken in 5.0 M NaCl at pH 2.0 under 1 atm Cl_2 (CER) or in 1.0 M H_2SO_4 under 1 atm O_2 (OER). No correction was performed for the resistance of the Pt electrodes, due to the low resistivity (< 0.0001 Ω/cm) of Pt. For 5.0 M NaCl at pH 2.0, a solution resistance of 3.45 ± 0.02 Ω was

measured. For 1.0 M H_2SO_4, a solution resistance of 1.91 ± 0.02 Ω was measured. These values were used to correct the electrodes for the IR drop. No correction was made for the electrode resistivity, as it is an intrinsic electrode property. Typical corrections from solution resistance were ~1.4 mV and ~0.3 mV for the OER at 10 mA/cm^2_{geo} and the CER at 1 mA/cm^2_{geo} respectively.

The system resistance was also measured as described above, but instead of Pt wire TiO_2 coated IrO_2, RuO_2, and FTO electrodes were used as the working electrodes. The measured solution resistance was a lower bound for the system resistances (Fig. S8). Data was not corrected for system resistance because this is an intrinsic property of the electrode. Neither the magnitude nor the shape of the change in overpotential or specific activity shown in Fig. 1 were explained by the magnitude or the pattern of the system resistivity which would have resulted in corrections of < 10 mV for the OER and < 3 mV for the CER.

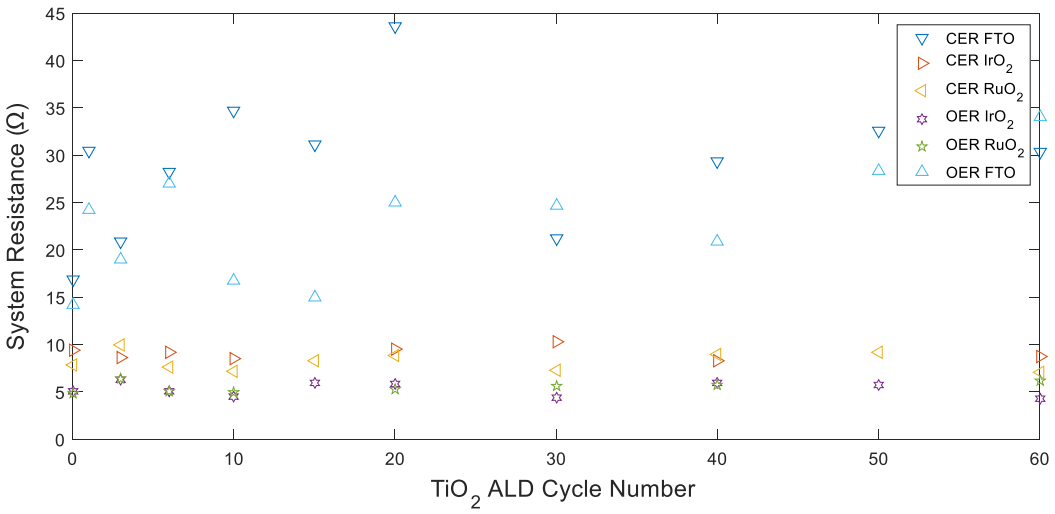

Fig. S8. System resistance as measured by electrochemical impedance spectroscopy in 5.0 M NaCl at pH 2.0 (CER) and 1.0 M H_2SO_4 (OER). The resistivity of the system did not appreciably change between 0 and 60 ALD cycles of TiO_2. For IrO_2 based electrodes, the average system resistance was 9.1 ± 0.6 Ω for CER condtions and 5.4 ± 0.6 Ω for OER conditions. For RuO_2 based electrodes, the average system resistance was 8.0 ± 1.0 Ω for CER condtions and as 5.3 ± 0.7 Ω for OER conditions. For FTO-based electrodes, the average system resistance was 30 ± 7 Ω for CER condtions and 23 ± 6 Ω for OER conditions.

Determination of Specific Activities

Determination of the Double-Layer Capacitance and Electrochemically Active Surface Area

In order to make a fair comparison between values herein and in the benchmarking study, the double-layer capacitance (C_d) was measured and linearly related to the electrochemically active surface area (ECSA) by Eq. S1 in the same manner as described in the benchmarking literature [21]. For the OER, briefly, C_d was measured by plotting the non-Faradaic current vs scan rate and extracting the slope of the linear best-fit line. An initial CV was conducted to identify the non-faradaic region, which in general was a 50 mV window around the open-circuit potential (E_{oc}). Scans were then conducted at scan rates of 0.005, 0.01, 0.025, 0.05, 0.1, 0.2, 0.4, and 0.8 V/s and 100% of the current was collected for each step (Fig. S9). Between potential sweeps, the working electrode was held at E_{oc} for 30 sec. The non-faradaic current at E_{oc} for each scan rate was plotted versus scan rate (Fig. S9). The average of the absolute value of the positive and negative slopes of the linear fits of the data was taken to be C_d. Because of the narrow potential window between oxidation of Cl^- and reduction of Cl_2, C_d was determined from electrochemical impedience spectroscpy at E_{oc}. Nyquist plots were fit to a resistor in series with a parallel combination of a capacitor and a shunt resistor (Fig. S10). The resulting capacitance was taken as the C_d. In both cases C_d values were used as described previously to calculate the ECSA [21]. Briefly, C_d was divided by the specific capacitance (C_s) of an average metal substrate in an acidic electrolyte (Table S4, Eq. S1). Few literature values exist for C_s in concentrated acidic brine, and C_s does not change apprecaibly with ionic strength for H_2SO_4. Both the CER and OER electrolytes were acidic, so the same value of C_s was used to calculate the ECSA for both the CER and OER:

$$\text{ECSA} = C_d / C_s \qquad \text{Eq. S1}$$

where C_S is specific capacitance (i.e., 0.035 mF/cm^2 for 1.0 M H_2SO_4 and 5.0 M NaCl, pH 2.0). To ensure mutual comparability, we chose the same C_s value that was used in the benchmarking literature for the OER [21].

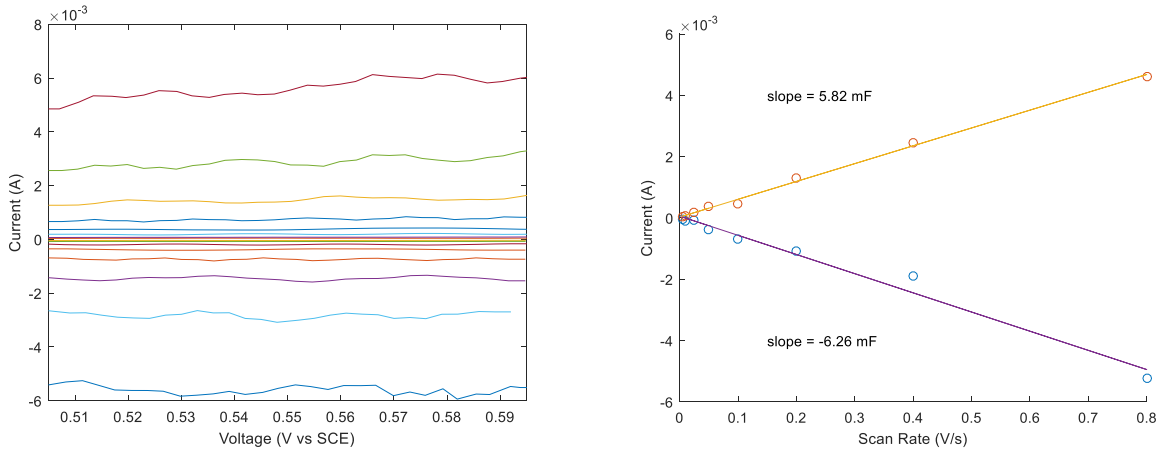

Fig. S9. Example double-layer capicitance measurements for determining ECSA for IrO_2 with 10 cycles of ALD TiO_2 in 1.0 M H_2SO_4. (Left) Linnear sweep voltamogramms in the non-Faradaic region at 0.005, 0.01, 0.025, 0.05, 0.1, 0.2, 04, and 0.8 V/s. (Right) Cathodic (yellow disks) and anodic (blue disks) charging currents measured at 0.55 V vs SCE plotted as a function of scan rate.

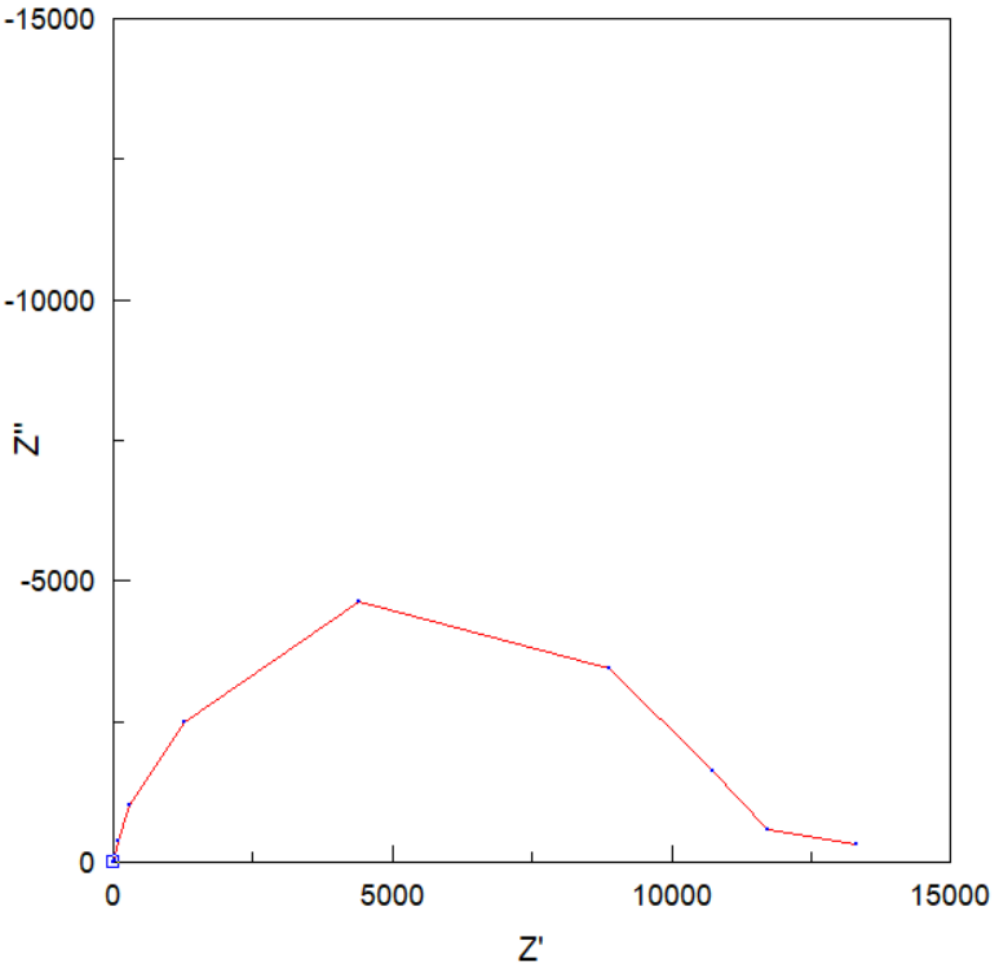

Fig. S10. Example impedence spectroscopy for IrO_2 with 0 cycles of ALD TiO_2 in 5.0 M NaCl pH 2.0 at E_{oc}. These data were fit to a resistor in series with a parallel combination of a capacitor and a shunt resistor. The resulting capacitance was taken as the C_d which in this case was was 3.24×10^{-6} F.

Table S4. Roughness factors (RFs) for IrO_2, RuO_2, and FTO based catalysts in 1.0 M H_2SO_4 and 5.0 M NaCl, pH 2.0. RFs are calculated by dividing the electrochemcially active surface area by the geometric surface area.

CER Catalyst Roughness Factors (RF)								
IrO_2	RF	error	FTO	RF	error	RuO_2	RF	error
0	1.86	0.06	0	0.16	0.01	0	0.98	0.07
1	2.01	0.04	1	0.16	0.01	3	1.28	0.05
3	2.51	0.02	3	0.15	0.03	6	1.20	0.06
6	1.41	0.02	6	0.16	0.04	10	0.84	0.06
10	1.13	0.05	10	0.15	0.02	20	1.49	0.08
20	1.20	0.01	15	0.17	0.02	30	1.77	0.04
40	1.03	0.02	20	0.15	0.02	40	1.89	0.06
60	0.31	0.03	40	0.14	0.01	60	2.06	0.07
			60	0.13	0.02			
OER Catalyst Roughness Factors (RF)								
IrO_2	RF	error	FTO	RF	error	RuO_2	RF	error
0	3.64	0.01	0	0.52	0.04	0	2.40	0.04
3	3.67	0.04	3	0.72	0.05	6	3.57	0.03
6	3.19	0.01	6	0.48	0.03	10	5.2	0.5
10	2.83	0.01	10	0.35	0.03	20	6.1	0.9
20	3.53	0.08	20	0.55	0.04	40	3.7	0.4
40	3.3	0.1	30	0.72	0.05	60	0.68	0.03
50	1.08	0.02	40	0.51	0.04			
60	0.55	0.01	60	0.31	0.02			

For most FTO based catalysts and some other catalysts with > 40 TiO_2 cycles, roughness factors of less than one were measured. ECSA is a measure of a surface's ability to charge the double layer. It is common for semiconductors to only have certain areas that are able to conduct charge (i.e. specific crystal facets, or areas around dopants), and therefore not the entire surface of a material may contribute to the ECSA. For highly active catalysts, like IrO_2 and RuO_2, usually ECSA values are above 1 (ours are between 2 and 4). For weaker, very flat catalysts (e.g. the FTO based catalysts studied here), roughness factors less than one are common for inactive catalysts and generally mean that large parts of the surface of the catalyst are either not conductive or are not electrocatatytically active [29, 30].

Calculating Specific Activities Using ECSA and AFM

As discussed in detail in prevous reports, reporting overpotential data relative to geometric current density can be misleading because geometric overpotentials can be influenced both by the roughness and the intrinsic activty of the catalyst [19, 20]. When assessing the strength of a catalyst it is important to separate the effects of having a rough substrate, and therefore more active catalyst area per unit geometric area, and having an intrinsically more active catalyst[19, 21, 28]. As is discussed in detail in previous work, roughening an electrode is an important engineering challenge, but the performance of a rough electrode will always be limited by the intrinsic charge transfer kinetics of the catalyst at high current densities[19, 20]. Comparing a catalyst's activity by normalizing the current to the geometric surface area of an electrode assumes that rough electrodes are perfectly flat and therefore often overestimates the performance of catalysts on rough electrodes, as shown in the benchmarking literature[19, 21, 28]. The most common way to compare catalyst activity is by measuring the electrochemically active surface area (ECSA) of a catalyst and normalizing the current density to the ECSA. Additionally, if a catalyst is very rough, there can be large errors in the ECSA, so it is important to make a very flat catalyst, as well as measure the ECSA, to not overestimate catalytic activity due to roughness[19, 21, 28].

To make the best effort to disentangle roughness from catalytic activity, we chose to make catalysts on very flat (i.e. bad) electrodes. As such, our roughness factors (the ratio of ECSA to geometric surface area) were between 2 and 4 for IrO_2 and RuO_2 based catalysts while, due to the use of glassy carbon instead of atomically flat (100)-oriented silicon as a substrate, roughness factors for the benchmarking catalysts were between 50 and 200 for the same catalysts prepared using the same recipe[21, 28]. When normalized to geometric surface area, > 400 mV of overpotential was required to reach 10 mA/cm^2 for the RuO_2 or IrO_2 based catalysts. These overpotentials are substantially higher than the much rougher RuO_2 and IrO_2 catalysts in the benchmarking literature. However, when current is normalized to ECSA, the activities of the bare RuO_2 and IrO_2 catalysts investigated herein agree very well with the activities of the RuO_2 and IrO_2 benchmarking catalysts, while the thinly coated RuO_2 and IrO_2 catalysts measured herein are considerably more active (Fig. 2) than the uncoated material. Furthermore, comparing the overpotential for the bare RuO_2 and IrO_2 catalysts investigated herein to reach 10 mA/cm^2 to the overpotential for similarly made catalysts to reach the same current density, the geometric overpotential agrees well with previously reported catalysts[31].

Atomic force microscopy can provide a more accurate picture of surface roughness than geometric surface area. However, this technique tends to underestimate surface roughness

because the AFM probe cannot reach steep, narrow valleys (e.g. AFM underestimated our Ir and Ru based catalyst roughness by a factor of 2-4 relative to ECSA). ECSA is generally more accepted because it is actually related to electrochemical properties of the electrode. We did however measure the AFM-based surface area because we wanted to compare our catalyst to the highly active IrO_x/SrO_x catalyst from Jaramilo's work[20]. The IrO_x/SrO_x catalyst had a Tafel slope for the OER of around 40 mV/dec indicating, that the IrO_x/SrO_x catalyst performs OER via a novel mechanism and therefore is more active than the catalyst investigated herein. However, ECSA data are unavailable for the IrO_x/SrO_x catalyst and we cannot compare our catalysts based on this metric. Therefore our catalyst has the highest activity for any catalyst based on ECSA alone.

Specific activities (Fig. 1 of main text) were calculated as previously described, by normalizing the current from cyclic voltamagrams to the electrochemically active surface area [21]. For RuO_2 and IrO_2 based catalysts, specific activities were calculated at 350 mV overpotential for the OER, and at 150 mV overpotential for the CER. For FTO, specific activities were calculated at 900 mV overpotential for the OER, and at 700 mV vs NHE for the CER.

Alteratively, specific activities were calculated by normalizing the measured current density to the topographic surface area measured by atomic force microscopy (AFM; see AFM section) for direct comparison with catalysts reported by Seitz et al [20]. Roughness factors for these calculations are reported in Table S1.

Tafel Analysis

Tafel data is shown in Fig. S11 below. IrO_2 + ALD TiO_2 catalysts is from this work and tafel data for $SrIrO_3$ catalyts is from previous work. Current density is shown for surface area as measured by AFM.

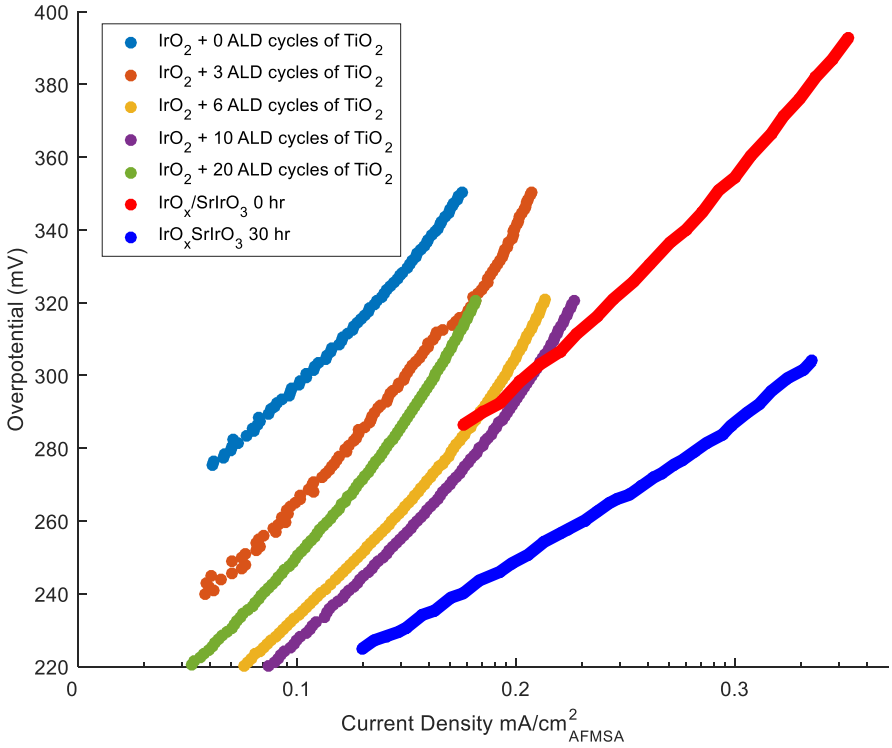

Fig. S11. Tafel plots from IrO_2 coated with 0 (dark blue), 3 (orange), 6 (yellow), 10 (purple), and 20 (green) ALD cycles of TiO_2 all from this work are shown next to those of $IrO_x/SrIrO_3$ at 0 (red) and 30 (light blue) hrs of activation as taken from literature [20]. To calculate the current density, the surfcae area was measured by AFM (table S1).

Table S5. A summary of the Tafel slopes and exchange current densities from this work (IrO_2 + TiO_2 catalyts) and previous work ($SrIrO_3$ catalysts) [20]. All current density data reported here is based on surfcae area that is measured by AFM (Table S1).

Catalyst	i_0 (mA/cm^2_{AFMSA})	slope ($mV/mA/cm^2_{AFMSA}$ decade)
IrO_2 + 0 ALD cycles of TiO_2	1.0×10^{-7}	59
IrO_2 + 3 ALD cycles of TiO_2	8.0×10^{-6}	65
IrO_2 + 6 ALD cycles of TiO_2	2.0×10^{-5}	64
IrO_2 + 10 ALD cycles of TiO_2	2.0×10^{-5}	61
IrO_2 + 20 ALD cycles of TiO_2	8.0×10^{-6}	61
$IrO_x/SrIrO_3$ 0 h	7.0×10^{-6}	57
$IrO_x/SrIrO_3$ 30 h	3.0×10^{-7}	38

The activated $IrO_x/SrIrO_3$ catalyst exhibits a previously unobserved Tafel slope that is lower than than known OER Tafel slopes (Table S5), and is therefore more active at industrially relevant current densities than any catalyst studied in this work.

To provide information about the reaction mechanism for the OER and CER, Tafel slopes were measured for all CER and OER catalysts. Table S6 lists the Tafel slopes for catalysts with 0 ALD cycles of TiO_2, the number of TiO_2 cycles resulting in the highest activity for that catalyst; and 40 ALD cycles of TiO_2. After addition of TiO_2, the Tafel slopes remained approximately constant until the catalysts lost activity, and the Tafel slopes deteriorated considerably at > 40 ALD cycles of TiO_2.

Table S6: A summary of the Tafel slopes for selected catalysts for the OER and CER.

Reaction:	OER		CER	
	TiO_2 Cycle Number	Tafel Slope (mV/dec)	TiO_2 Cycle Number	Tafel Slope (mV/dec)
IrO_2	0	59	0	38
	10	61	3	36
	40	63	40	39
RuO_2	0	68	0	30
	10	63	40	34
	40	70		
FTO	0	198	0	196
	30	216	10	193
	40	193	40	206

Determination of E_{ZC} by Electrochemical Impedance Spectroscopy

To ensure high capacitance values, 5.0 M $NaNO_3$ at pH 2.0 was prepared by dissolving $NaNO_3$ (J.T. Baker, Center Valley, PA, 99.6%, used as received) in 900 mL of water (18 MΩ cm, Millipore, Billerica, MA), adjusting the pH using HNO_3 (Sigma Aldrich, $\geqslant$ 60%, used as received), and diluting with water to 1 L. Working electrodes were prepared as described above. A working electrode, an SCE reference electrode (CH instruments), a coiled platinum wire counter electrode (Sigma Aldrich), and 20 mL of $NaNO_3$ solution were added to a 25 mL 4 neck 14/20 round bottom flask reactor. The reactor was gently bubbled with N_2 for at least 15 min before experiments, as

well as during experiments. The impedance was measured using a Bio-Logic potentiostat/galvanostat model VSP-300 with EIS capability. All studies were performed at 25 ± 2 °C. Impedance spectra were recorded in the frequency range of 1 MHz to 10 mHz, with a modulation amplitude of 5 mV. An initial potential range of 1.1 to 0 V vs SCE, with a step size of 25 mV, was performed to identify the E_{ZC} region. A narrower potential range (typically ± 200 mV around the apparent E_{ZC}) was then used to measure the E_{ZC} value.

EIS data were fit as described previously, using *ZView* software, to an R_s-(R_p-C) circuit, where R_s is solution resistance at high frequencies, *C* is capacitor that represents double-layer capacitance in mid-range frequencies, and R_p is charge transfer resistance at low frequencies (Figs. S12 and S13) [20].

As previously reported, for FTO, IrO_2, and RuO_2 the capacitance values extracted from impedance spectroscopy are expected to approximate a traditional double layer capacitance (C_{DL}) to first order [21, 22]. For samples with partial, semi-continuous and continuous TiO_2 coatings (Fig. S1-3), the TiO_2 layers are so thin for reasonably active catalysts (< 1.95 nm or 30 ALD cycles of TiO_2), the TiO_2 is assumed to be fully carrier-depleted within the potentials in question, so the changes in C_{DL} measured by impedance may be used to approximate a traditional E_{ZC}.

To confirm this assumption, Mott-Schottky analysis of the capacitance data was performed for the various samples. For an equivalent circuit comprising a series resistor combined with a parallel combination of a capacitor (*C*) and a shunt resistance, the inverse of the square of the capacitance (Farads) taken from the fit of the full frequency range on the nyquist plots was plotted against the potential with respect to NHE, E_{NHE}. For the low-cycle numbers of ALD TiO_2 on the substrates, a local maximum was observed, corresponding to the local minimum of *Q* vs $E_{NHE,}$ and thus the E_{ZC}. However, for samples in which 100 or 1000 cycles of ALD TiO_2 were deposited, corresponding to ~6.5 and ~65 nm respectively, a linear plot from Q^{-2} vs E_{NHE} was obtained. These plots were analyzed through application of the Mott-Schottky equation (Eq. S2), where ε_0 is the permittivity of free space, ε is the specific permittivity of TiO_2, *A* is the area of the electrode, *q* is the (unsigned) charge on an electron, N_d is the dopant density, V_{fb} is the flat band potential, k_b is the Boltzmann constant, *T* is temperature, and *V* is the applied potential, and *C* is the capacitance.

$$\frac{1}{C^2} = \frac{2}{\varepsilon\varepsilon_0 A^2 q N_d}\left(V - V_{fb} - \frac{k_b T}{q}\right) \qquad \text{Eq. S2}$$

From the 500 and 1000 TiO_2 ALD cycle samples, a value of N_d = (8.1 ± 4.2) X 10^{19} cm^{-3} was found, and the flat-band potential for the TiO_2, V_{fb}, was calculated to be 282 ± 15 mV positive of NHE. From these parameters, in conjunction with Eq. S3 and at an applied potential of 0.25 V vs NHE (the lowest E_{ZC} value), the TiO_2 in question would have a depletion width of 7.3 ± 1.4 nm, which is substantially higher than the actual thickness of TiO_2 present in any of the catalytically relevant samples analyzed here (< 60 TiO_2 ALD cycles, or less than 3.9 nm).

$$W = \sqrt{\frac{2\varepsilon\varepsilon_0 V_{bi}}{qN_d}} \qquad \text{Eq. S3}$$

Within the framework of this analysis, the TiO_2 film deposited on the substrates is under full depletion throughout the course of these experiments, and the capacitive effects from this film may therefore be ignored when the potential of zero charge is calculated by impedance spectroscopy.

Because E_{ZC} is believed to be a fundamental property of a material, changing the electrolyte may change the absolute value of the E_{ZC}, but should not change the trend in the values of materials measured in the same electrolyte [23].

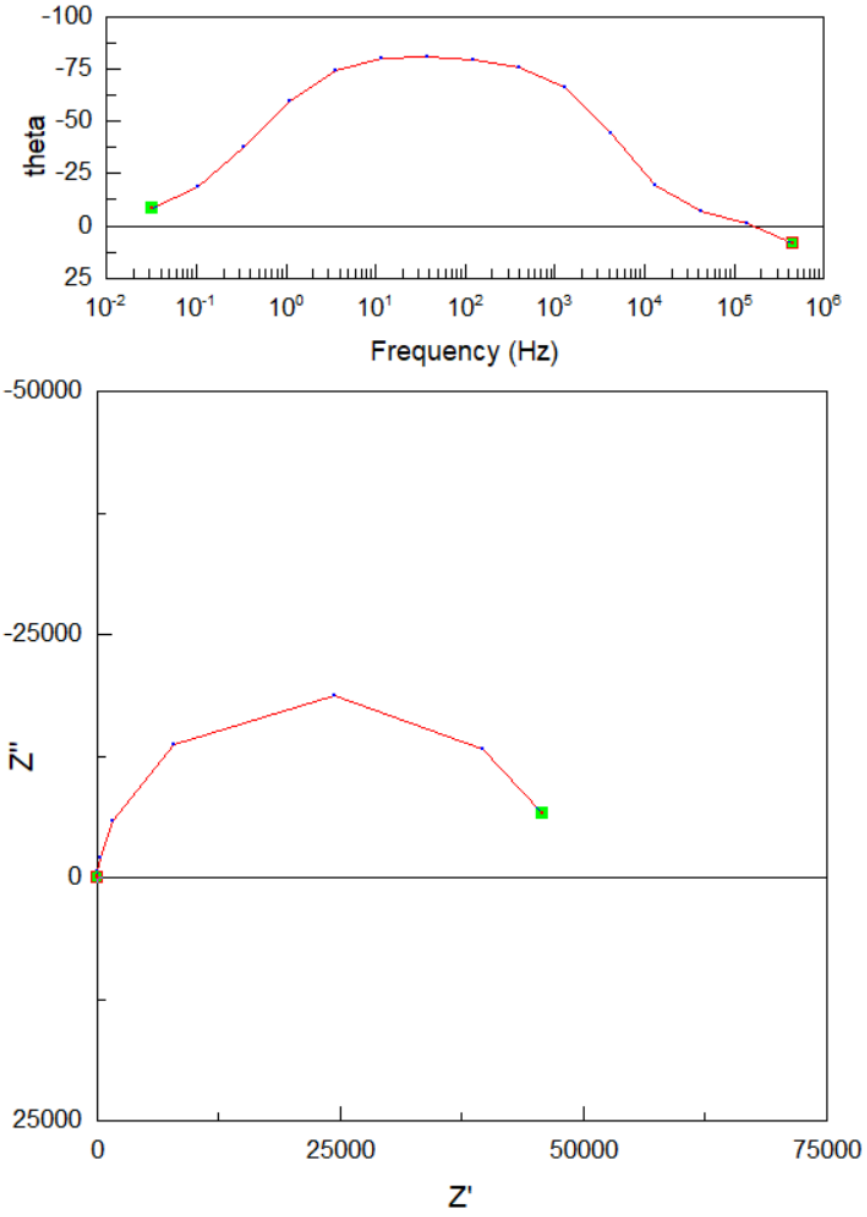

Fig. S12. Sample Bode (above) and Nyquist (below) plots of electrochemical impedence spectroscopy data of IrO_2 coated with 10 ALD cycles of TiO_2. The Bode plot shows the frequency of the alternating current signal (Hz) versus the phase shift of the impedance response (degrees). The Nyquist plot shows the real (*Z*') and imaginary (*Z*") components of the impedance response to the alternating current signal. Data presented in the figure were collected at 105 mV vs SCE in 5.0 M $NaNO_3$ at pH 2.0. The resulting equivelent circuit [R_s-(R_p-*C*)] fit of these data yielded a capacitance of 5.8× 10^{-6} F.

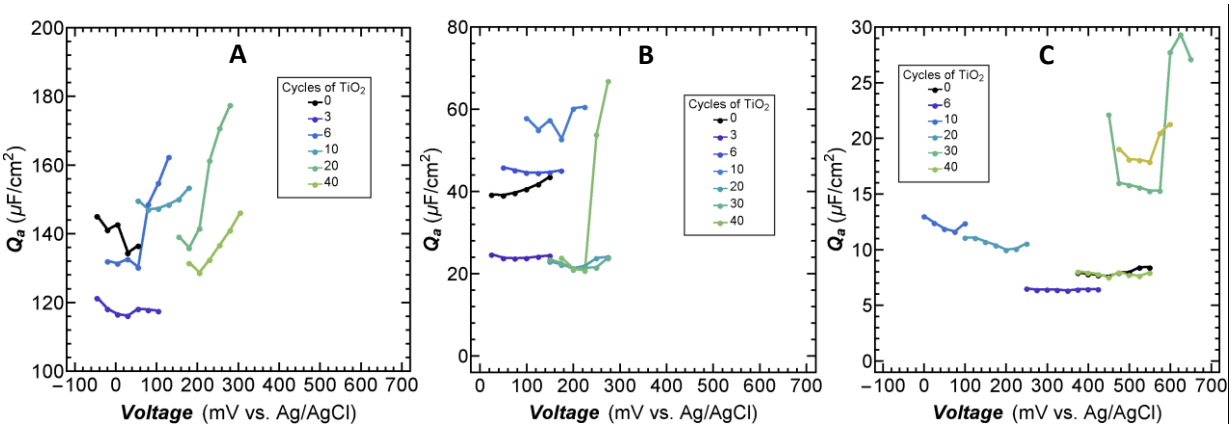

Fig. S13. Electrochemical impedance spectroscopy of (A) IrO_2, (B) RuO_2, (C) and FTO coated with various ALD cycles of TiO_2 at 25 mV intervals in 5.0 M $NaNO_3$ at pH 2.0. The resulting Nyquist plots were modeled as R_s-(C-R_p) circuits. The calculated capacitance values (dots) for each sample (set of dots) are shown here. The minimum value of each curve represents the E_{ZC}. The magnitude of the capacitance represents the surface area of the sample.

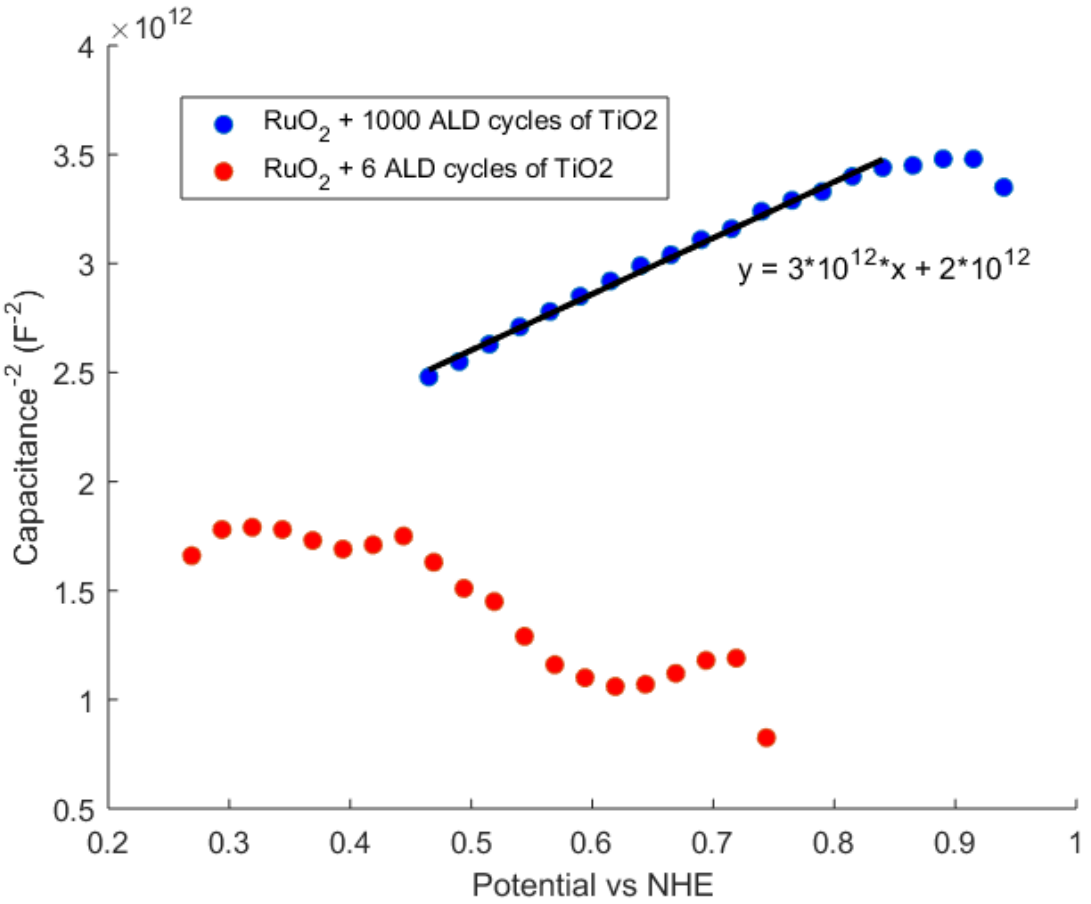

Fig. S14. Sample Mott-Schottky (E vs $1/C^2$) plots of RuO_2 with 0 (red), 1000 (blue) ALD TiO_2 cycles. The fit, using a geometric surface area of 7.1 X 10^{-6} m^2, yielded N_d = of 5.4 X 10^{19} cm^{-3}.

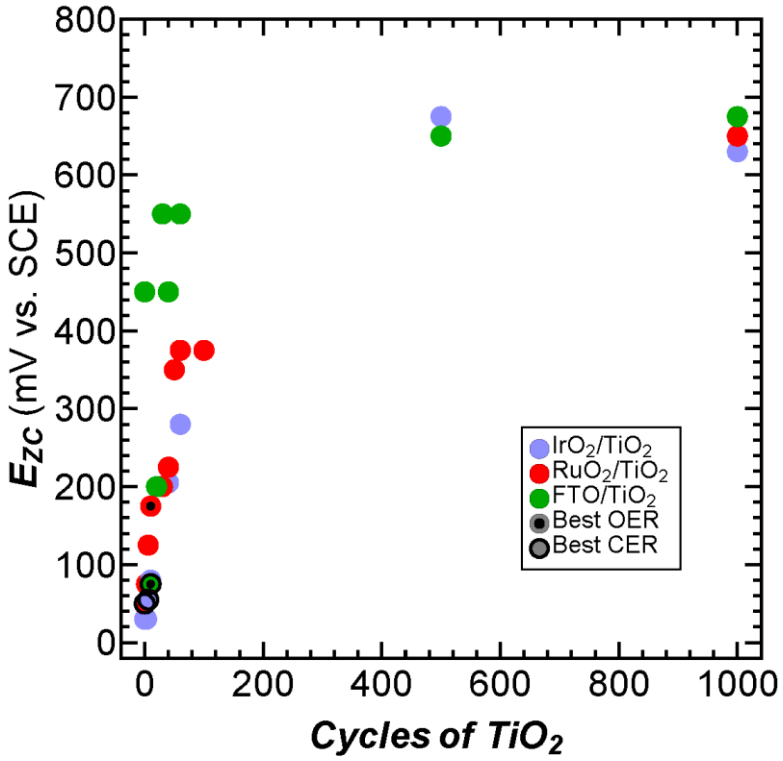

Fig. S15. Potential of zero charge as a function of TiO_2 cycle number for IrO_2, RuO_2, and FTO electrocatalysts. Black dots and disks with black borders indicate the catalysts with the highest specific activity for each substrate for the OER and CER, respectively.

For thick (>100 cycles) ALD TiO_2 films, the E_{ZC} values converged, indicating that all surfaces were electronically similar, bulk TiO_2. For The CER, the most active catalysts had E_{ZC} values of ~55, ~50, and ~75 mV vs SCE (IrO_2 + 3 ALD TiO_2 cycles, RuO_2 + 0 ALD TiO_2 cycles, and FTO + 10 ALD TiO_2 cycles respectively) and for the OER the optimal E_{ZC} was ~80, ~175, and ~75 mV vs SCE (IrO_2 + 10 ALD TiO_2 cycles, RuO_2 + 10 ALD TiO_2 cycles, and FTO + 10 ALD TiO_2 cycles respectively) (Figs. 3 and S15).

X-ray Photoelectron Spectroscopy

Data Collection and Peak Fitting

X-ray photoelectron spectroscopy (XPS) data were collected using a Kratos AXIS Ultra spectrometer (Kratos Analytical, Manchester, UK) equipped with a hybrid magnetic and

electrostatic electron lens system, a delay-line detector (DLD), and a monochromatic Al K□ ± X-ray source (1486.7 eV). Data were collected at pressures of ~2 x 10^{-9} Torr with photoelectrons collected along the sample surface normal. The analyzer pass energy was 80 eV for survey spectra and 10 eV for high-resolution spectra, which were collected at a resolution of 50 meV. The instrument energy scale and work function were calibrated using clean Au, Ag, and Cu standards. The instrument was operated by Vision Manager software v. 2.2.10 revision 5.

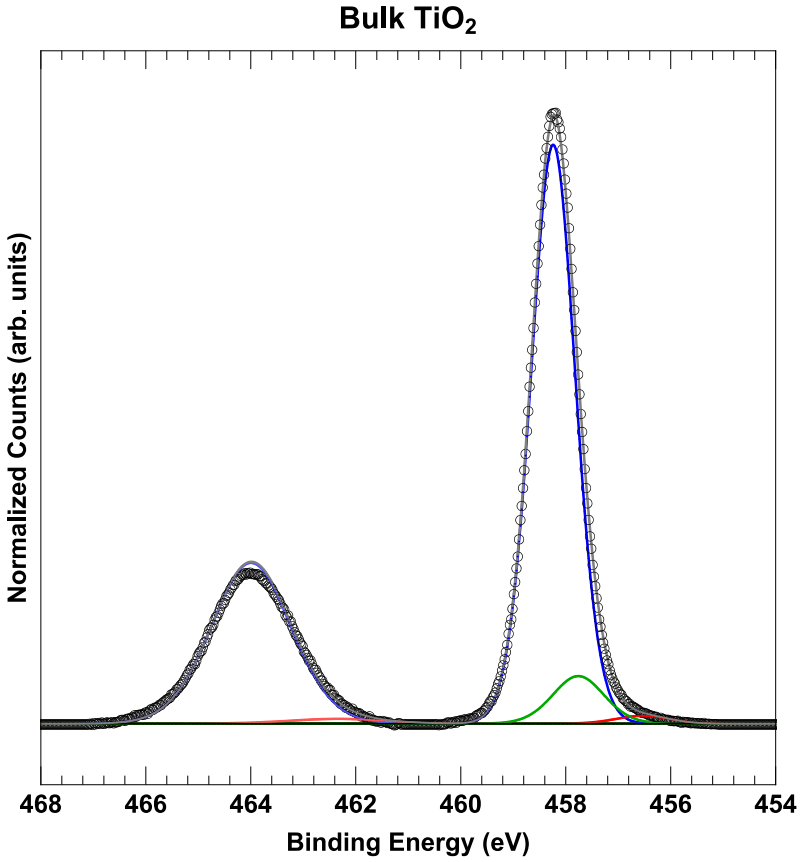

Fig. S16. X-ray photoelectron spectroscopy of the Ti 2p region for a bulk TiO_2 film. The peak associated with Ti^{4+} is shown in blue. The slightly and highly reduced Ti peaks are shown in green and red, respectively, and the most highly oxidized Ti peak is shown in orange.

XPS data were analyzed using CasaXPS software (CASA Software Ltd). The Ti 2p core-level photoemission spectra were fit constraining the peak separation and the peak area ratio between Ti $2p^{3/2}$ and Ti $2p^{1/2}$ peaks to 5.75 eV and 2:1, respectively. The peak area ratios were allowed to deviate 5% from the 2:1 ratio to account for inaccuracies in the background. All peaks were fit using a Gaussian-Lorentzian with 30% Lorentzian character. A bulk TiO_2 sample (1000 cycles) was used as a standard to determine the peak positions for the Ti $2p_{3/2}$ core-level photoemission

(Fig. S16). The bulk TiO_2 sample fit exhibited a main peak at 458.24 eV , which is consistent with reports of the peak position for TiO_2 and therefore was ascribed to the Ti^{4+} oxidation state, and two additional peaks at lower binding energies, 457.6 eV and 456.6 eV, respectively, associated with a more reduced Ti state, likely Ti^{3+}[24-27]. These peaks were propagated through for IrO_2 for all thicknesses of TiO_2. In addition to these peaks, a fourth peak at slightly higher binding energy (458.5 eV) was needed to fit the FTO spectra.

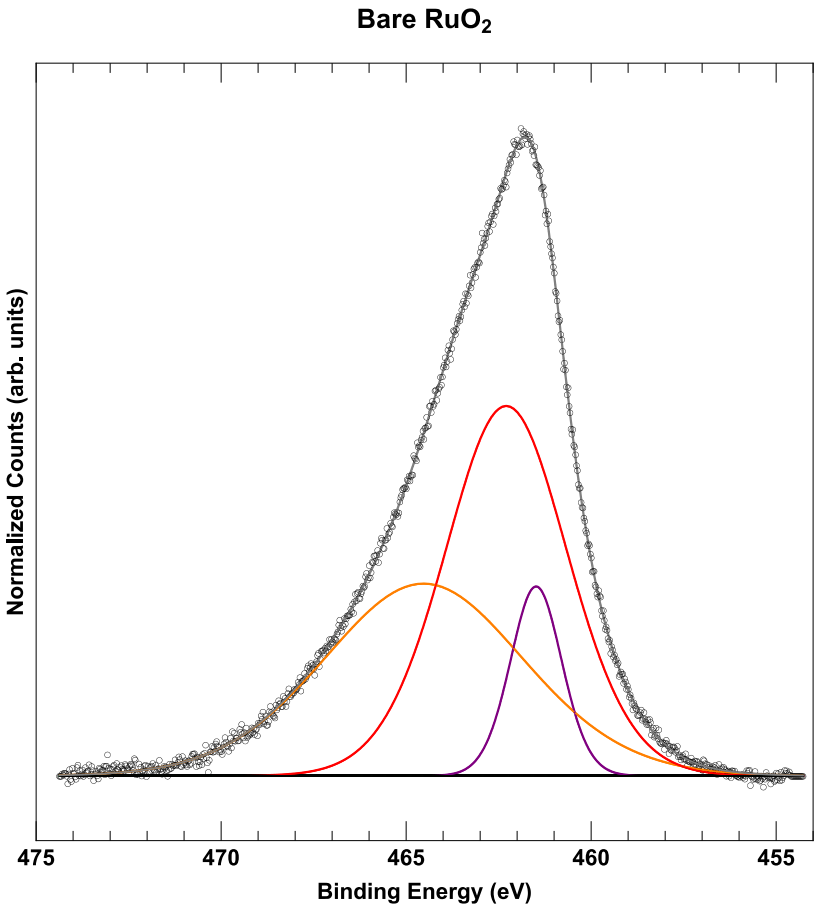

Fig. S17. X-ray photoelectron spectroscopy of the Ti 2p region for a bare RuO_2 film. The 3 orange, red, and purple peaks define the Ru 3p core level photoemission associated with RuO_2.

In the case of RuO_2, the Ru 3p core level exhibited a broad peak in the Ti 2p region (Fig. S17), which was well-fit by 3 Gaussian-Lorentzian peaks at 461.5 eV, 462.3 eV, and 464.5 eV, respectively. These Ru 3p core level photoemission peaks were propagated through for the fits of the spectra with ALD TiO_2. In addition to the 3 peaks associated with the Ru 3p core level, the spectra were also fit with the 3 peaks associated with bulk TiO_2, as described above. To

deconvolute the effect of Ru 3p core level photoemission from the TiO_2 signal, the Ru 3p core level peaks were subtracted from the spectra resulting in spectra corresponding purely to the Ti 2p core level photoemission.

The photoemission from the underlying metal oxide substrates was also measured. Peak fitting was performed on the bare metal oxide substrate and then propagated through to the spectra with ALD TiO_2. The Ir 4f and Ru 3d photoemission core-level spectra were fit according to previous reports in the literature [28, 29]

Ti 2p Core-level Photoemission

The full Ti 2p core-level photoemission region is shown in Fig. S18, stacked from bottom to top for increasing TiO_2 cycle number. Depositing low cycle numbers of ALD TiO_2 on IrO_2 and RuO_2 produced Ti core-level spectra containing lower binding-energy signatures than the bulk TiO_2 film, which we ascribe to mixed oxides in which the Ti is in a more reduced form, likely a Ti^{+3} oxidation state. The Ti oxidation state for these samples gradually increased to its bulk oxidation state (~+4) as cycle number increased and bulk TiO_2 was observed (Fig. 4). In the case of ALD TiO_2 on FTO, a different trend was observed in which the lower cycle number thicknesses produced spectroscopic signatures with binding energies primarily at the bulk position as well as a higher binding-energy peak. We ascribe this added peak to a mixed phase between the substrate (FTO) and the thin TiO_2 film, but one in which the chemical nature of the phase produces a seemingly more electron-poor film, and where the mixed phase is likely Ti^{4+}. The variation in oxidation state of the Ti species with TiO_2 thickness is accompanied by a shift in the overall Ti $2p_{3/2}$ peak position relative to a bulk (1000 cycles) TiO_2 film for IrO_2 and RuO_2 while the shift in the FTO peak position is less substantial and opposite in sign (Fig. S19).

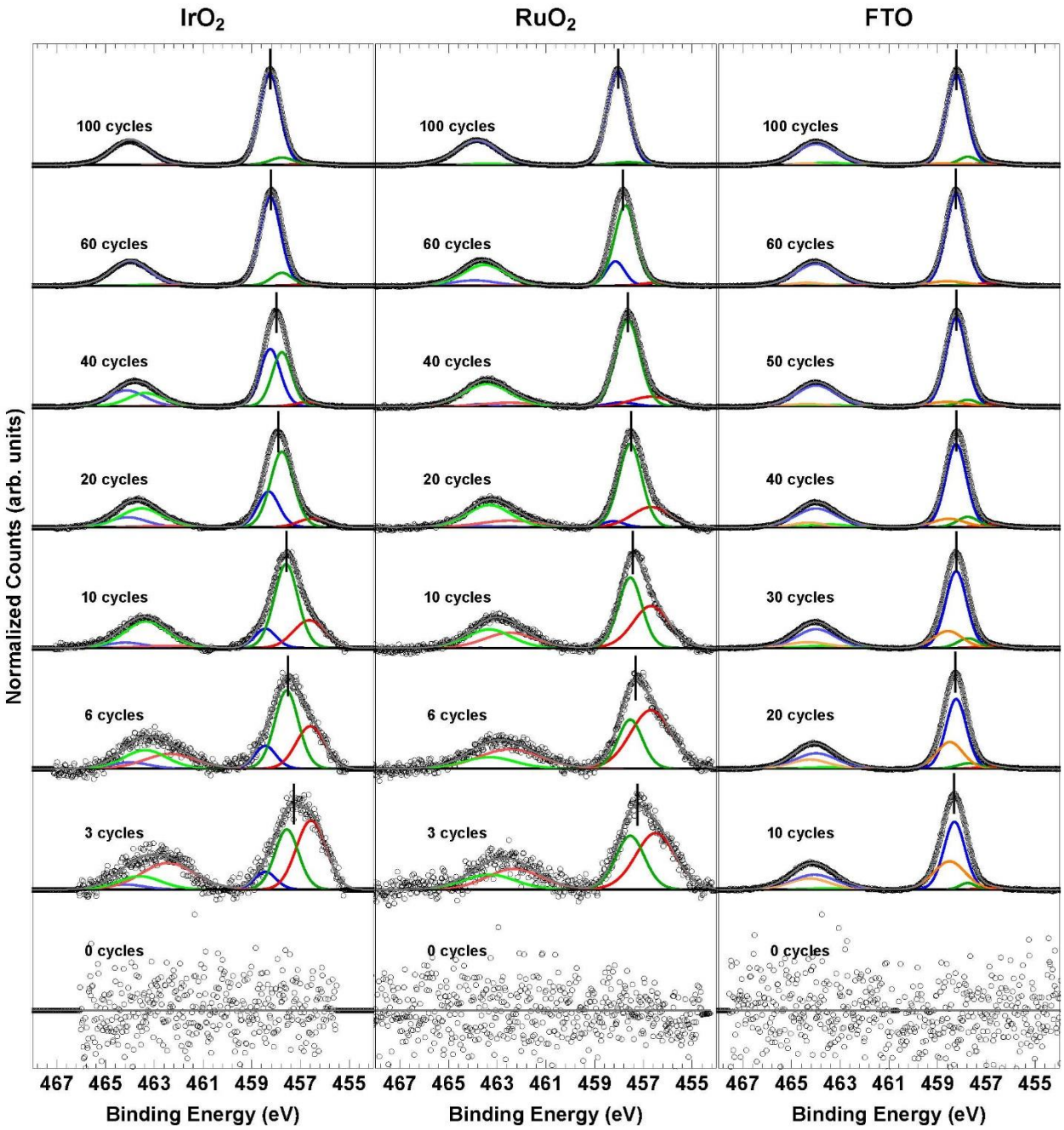

Fig. S18. X-ray photoelectron spectroscopy of the Ti 2p region for IrO_2, RuO_2, and FTO catalysts. Bulk TiO_2 is shown as the blue peak in each spectrum. The slightly and highly reduced Ti peaks are shown in green and red, respectively, and the most highly oxidized Ti peak is shown in orange.

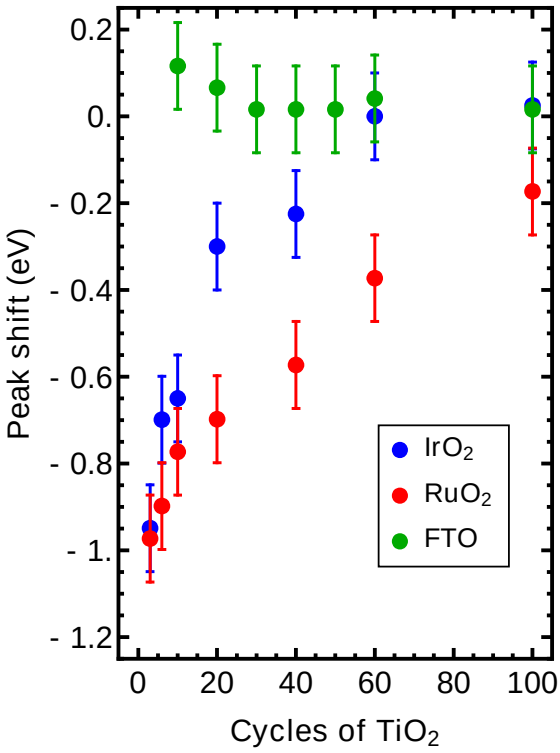

Fig. S19. Ti $2p_{3/2}$ overall peak shift relative to bulk TiO_2 as a function of TiO_2 cycle thickness for IrO_2, RuO_2, and FTO.

Underlying Metal Oxide Photoemission

The Ir 4f, Ru 3d, and Sn 3d core-level photoemission for the IrO_2-, RuO_2, and FTO-based catalysts is shown in Fig. S20, stacked bottom to top for increasing TiO_2 thickness. The spectra are fit according to the methods as described above with the blue and red shaded peaks representing the main peak and its satellite peak, respectively. The areal ratio of the main to satellite peak is tabulated in Table S7 for each catalyst at different TiO_2 thicknesses, with larger ratios indicating a relatively more reduced metal species. Upon initial TiO_2 deposition (3 cycles) the main to satellite areal ratio for IrO_2 and RuO_2 decreases indicating a more oxidized metal state relative to that of the bare substrate. In the case of FTO, deposition of 10 cycles of TiO_2 leads to a lower main to satellite peak ratio, indicating a slightly more reduced state relative to that of bare FTO. However, there is no discernable trend in either main to satellite peak ratio nor in the peak shift (Fig. S22) and it is likely that changes in the oxidation state of the underlying metal oxide are beyond the detection limit of our measurements.

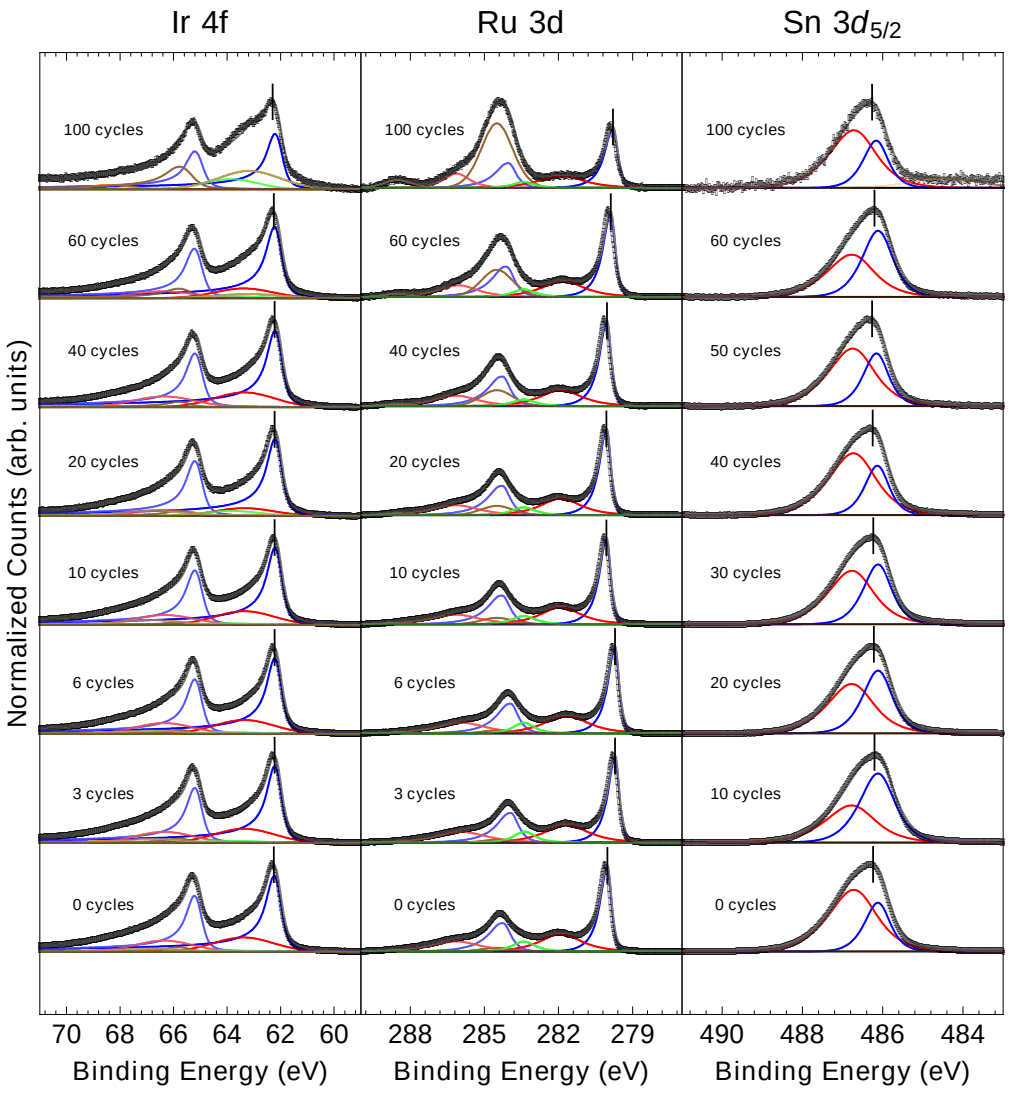

792

793

794 **Fig. S20.** X-ray photoelectron spectroscopy of the Ir 4f, Ru 3d, and Sn $3d_{5/2}$ region for IrO_2-

795 RuO_2- and FTO-based electrocatalysts as a function of TiO_2 thickness.

796

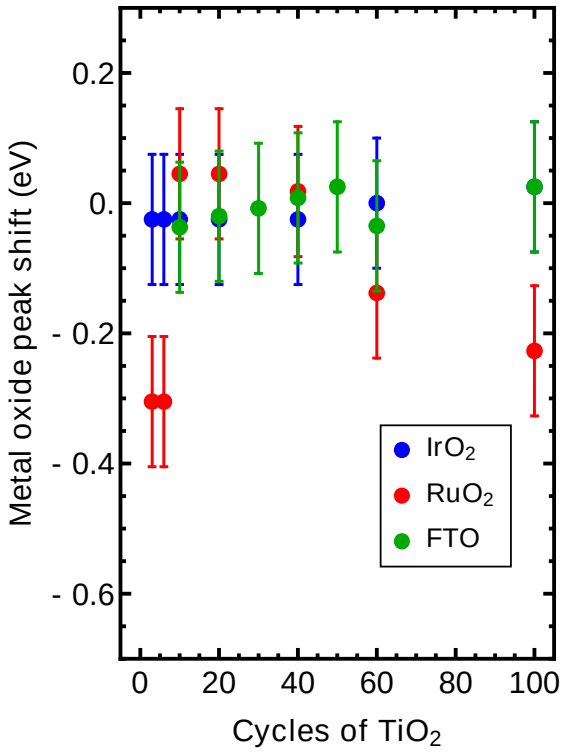

Fig. S21. Overall peak shift of the main peak of the Ir 4f, Ru 3d, and Sn $3d_{5/2}$ spectra relative to the bare metallic (0 cycle) metal-oxide substrate as a function of TiO_2 cycle thickness for IrO_2, RuO_2, and FTO, respectively.

Table S7. The areal peak ratios of the main peak to the satellite peak for the Ir 4f, Ru 3d, and Sn 3d core-level photoemission.

TiO_2 Cycles	Ir 4f	Ru 3d	Sn 3d
0	4.76	1.42	0.42
3	4.73	1.34	-
6	4.7	1.33	-
10	4.95	1.51	1.30
20	8.78	1.58	0.81
30	-	-	0.69
40	4.65	1.59	0.41
50	-	-	0.50
60	6.86	1.62	1.01
100	∞	1.52	0.435

Electrocatalyst Stability

X-ray photoelectron spectra were taken before and after 24-hour stability testing to understand the longevity of the catalytic enhancement. Figure S22 shows XPS spectra of the Ti 2p core-level before and after testing for the catalysts with the lowest overpotential for the OER for each materials system, 10 cycles, 10 cycles, and 30 cycles of TiO_2 for IrO_2, RuO_2, and FTO, respectively. After testing, no Ti species was detectable for any of the electrocatalysts tested in this study, which correlates well with the loss in catalytic performance over the duration of the stability test. The peak in the Ti 2p region for RuO_2 after testing is due to the Ru 3p core-level peaks and not to species associated with TiO_2. XPS spectra were also collected after 24-hour stability tests of the electrodes for the CER. Unlike for the OER, all electrocatalysts (except for the FTO based catalysts, which performed similarly as for the OER) showed stable performance over the duration of the stability test. XPS spectra after testing indicate that TiO_2 films are still present. A representative XPS spectra of the Ti 2p region for a RuO_2-based electrocatalyst before and after stability testing for the CER is shown in Fig. S24.

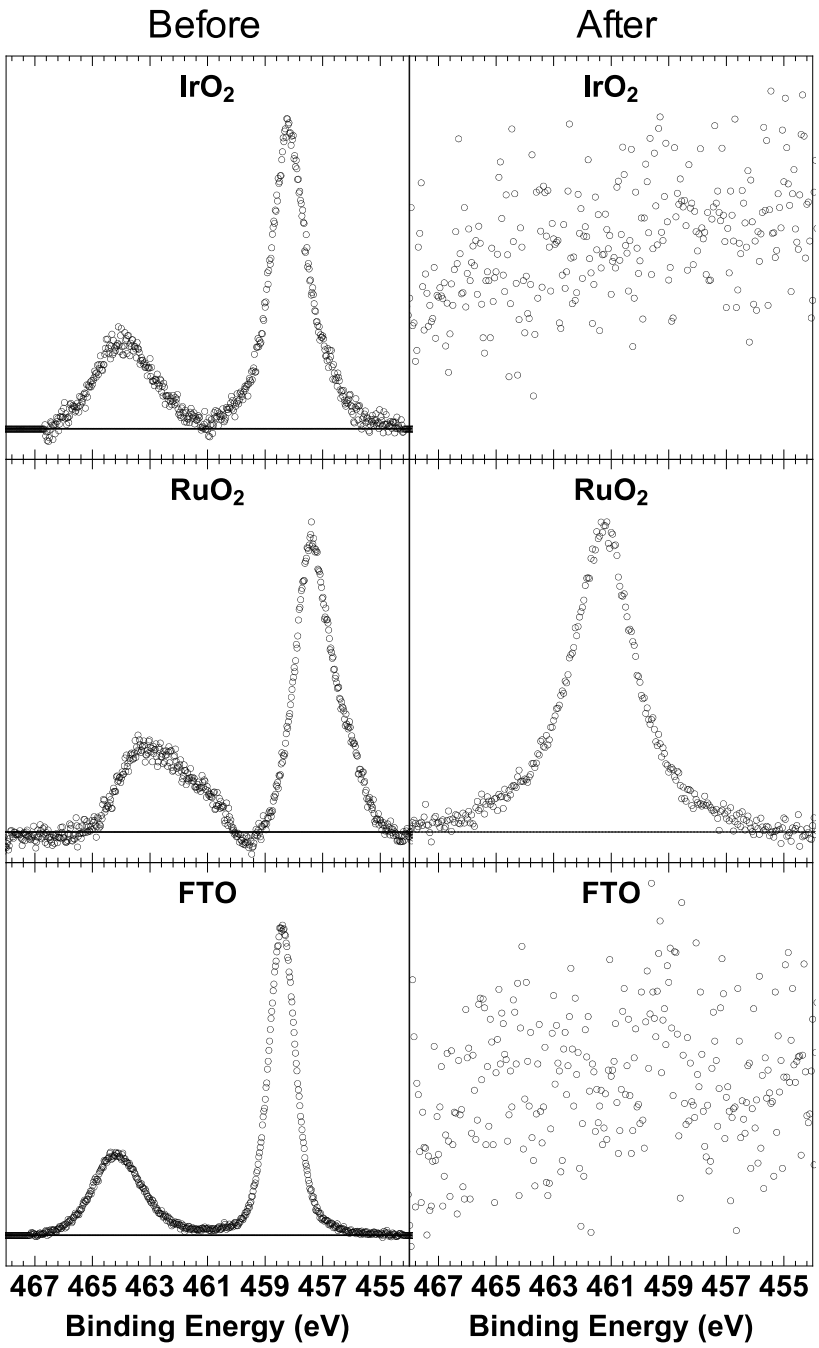

Fig. S22. X-ray photoelectron spectroscopy of the Ti 2p region for IrO_2, RuO_2, and FTO electrocatalysts with 10 cycles, 10 cycles, and 30 cycles of TiO_2, respectively, before and after stability testing for the OER. Note the peak still visible in the "after" RuO_2 spectra is associated with the Ru 3p core levels.

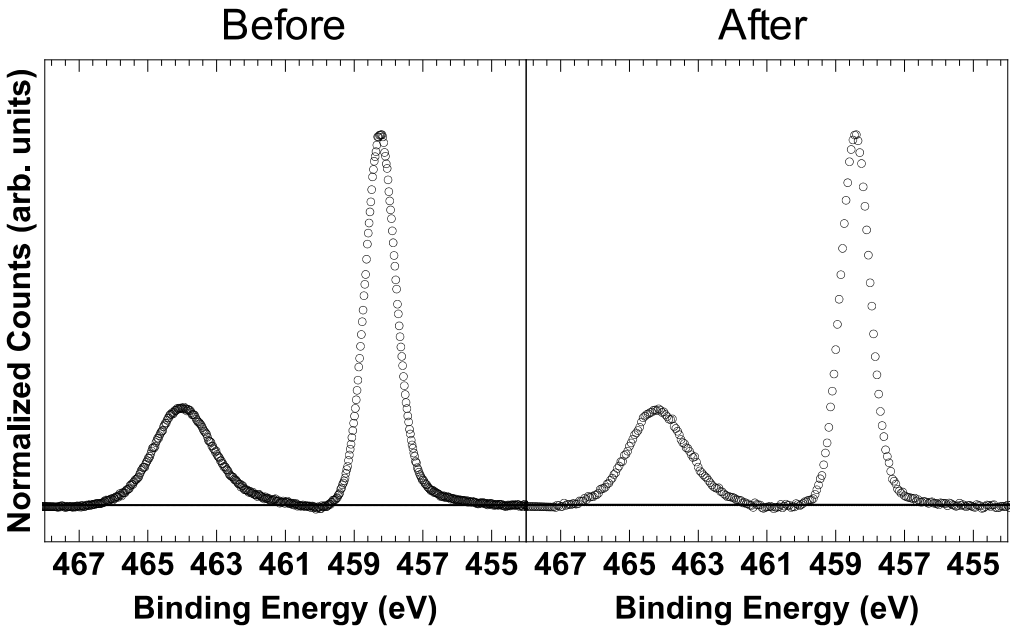

Fig. S23. X-ray photoelectron spectroscopy of the Ti 2p region for an RuO_2 electrocatalyst with 60 cycles of before and after 24-hour stability testing for the CER. The TiO_2 is still present after testing.

Notes and references:

1. B. R. Chalamala, Y. Wei, R. H. Reuss, S. Aggarwal, B. E. Gnade, R. Ramesh, J. M. Bernhard, E. D. Sosa and D. E. Golden, *Applied Physics Letters*, 1999, **74**, 1394-1396.
2. M. M. Jevtić, E. V. Jelenković, K. Y. Tong and G. K. H. Pang, *Thin Solid Films*, 2006, **496**, 214-220.
3. F. E. Akkad and S. Joseph, *Journal of Applied Physics*, 2012, **112**, 023501.
4. T. Uustare, J. Aarik, A. Aidla and V. Sammelselg, *Journal of Crystal Growth*, 1995, **148**, 268-275.
5. E. Verlage, S. Hu, R. Liu, R. J. R. Jones, K. Sun, C. Xiang, N. S. Lewis and H. A. Atwater, *Energy & Environmental Science*, 2015, **8**, 3166-3172.
6. R. T. Sanderson, *Journal of Chemical Education*, 1954, **31**, 2.
7. J. Noh, S. Back, J. Kim and Y. Jung, *Chemical Science*, 2018, **9**, 5152-5159.
8. L. R. Murphy, T. L. Meek, A. L. Allred and L. C. Allen, *The Journal of Physical Chemistry A*, 2000, **104**, 5867-5871.
9. J. B. Mann, T. L. Meek, E. T. Knight, J. F. Capitani and L. C. Allen, *Journal of the American Chemical Society*, 2000, **122**, 5132-5137.
10. L. C. Allen, *Journal of the American Chemical Society*, 1989, **111**, 9003-9014.
11. Z. W. Seh, J. Kibsgaard, C. F. Dickens, I. Chorkendorff, J. K. Nørskov and T. F. Jaramillo, *Science*, 2017, **355**, eaad4998.
12. L. C. Seitz, C. F. Dickens, K. Nishio, Y. Hikita, J. Montoya, A. Doyle, C. Kirk, A. Vojvodic, H. Y. Hwang, J. K. Norskov and T. F. Jaramillo, *Science*, 2016, **353**, 1011-1014.
13. C. C. L. McCrory, S. Jung, I. M. Ferrer, S. M. Chatman, J. C. Peters and T. F. Jaramillo, *Journal of the American Chemical Society*, 2015, **137**, 4347-4357.
14. C. E. Boman, *Acta Chem. Scand.*, 1970, **24**, 116-&.

15. A. A. Bolzan, C. Fong, B. J. Kennedy and C. J. Howard, *Acta Crystallogr. Sect. B-Struct. Commun.*, 1997, **53**, 373-380.
16. K. S. Pitzer and G. Mayorga, *The Journal of Physical Chemistry*, 1973, **77**, 2300-2308.
17. S. A. Angus, B; de Reuck, K M, *Chlorine: international thermodynamic tables of the fluid state*, Elsevier Science, Burlington, MA, 1985.
18. J. Jia, L. C. Seitz, J. D. Benck, Y. Huo, Y. Chen, J. W. D. Ng, T. Bilir, J. S. Harris and T. F. Jaramillo, *Nature Communications*, 2016, **7**, 13237.
19. American Public Health Association., American Water Works Association., Water Pollution Control Federation. and Water Environment Federation., *Journal*, 1960, volumes.
20. A. Łukomska and J. Sobkowski, *Journal of Electroanalytical Chemistry*, 2004, **567**, 95-102.
21. J. E. N. Swallow, B. A. D. Williamson, T. J. Whittles, M. Birkett, T. J. Featherstone, N. Peng, A. Abbott, M. Farnworth, K. J. Cheetham, P. Warren, D. O. Scanlon, V. R. Dhanak and T. D. Veal, *Advanced Functional Materials*, DOI: 10.1002/adfm.201701900, 1701900-n/a.
22. L. F. Mattheiss, *Physical Review B*, 1976, **13**, 2433-2450.
23. S. Trasatti, *Journal of Electroanalytical Chemistry and Interfacial Electrochemistry*, 1971, **33**, 351-378.
24. A. P. Dementjev, O. P. Ivanova, L. A. Vasilyev, A. V. Naumkin, D. M. Nemirovsky and D. Y. Shalaev, *J Vac Sci Technol A*, 1994, **12**, 423-425.
25. M. V. Kuznetsov, J. F. Zhuravlev and V. A. Gubanov, *J Electron Spectrosc*, 1992, **58**, 169-176.
26. F. Werfel and O. Brummer, *Phys Scripta*, 1983, **28**, 92-96.
27. D. Gonbeau, C. Guimon, G. Pfisterguillouzo, A. Levasseur, G. Meunier and R. Dormoy, *Surf Sci*, 1991, **254**, 81-89.
28. P. Verena, J. T. E., V. V. J. J., M. Cyriac, A. Rosa, T. Detre, G. Frank, S. Michael, G. M. T., A. Jasmin, H. Maike, W. Gisela, P. Simone, H. Michael, K. G. Axel and S. Robert, *Surface and Interface Analysis*, 2016, **48**, 261-273.
29. B. V. Crist, *Handbook of monochromatic XPS spectra*, Wiley, Chichester ; New York, 2000.